An Evaluation of ENSO Asymmetry in the Community Climate System Models: A View from the Subsurface

Tao Zhang[1], De-Zheng Sun[1], Richard Neale[2], and Phil Rasch[3]

[1]Cooperative Institute for Research in Environmental Sciences

University of Colorado/NOAA Earth System Research Laboratory

Physical Sciences Division

Boulder, Colorado

[2]National Center for Atmospheric Research, Boulder, Colorado

[3]Pacific Northwest National Laboratory, Richland, Washington

E-mail: tao.zhang@noaa.gov

dezheng.sun@noaa.gov

May 4, 2009

(Revised)

(Submitted to *Journal of Climate*)

Abstract

The asymmetry between El Niño and La Niña is a key aspect of ENSO, and needs to be simulated well by models in order to fully capture the role of ENSO in the climate system. Here we evaluate the asymmetry between the two phases of ENSO in five successive versions of Community Climate System Model (CCSM1, CCSM2, CCSM3 at T42 resolution, CCSM3 at T85 resolution, and the latest CCSM3+NR with Neale and Richter convection scheme). Different from the previous studies, we not only examine the surface signature of ENSO asymmetry, but also its subsurface signature. We attempt to understand the causes of the ENSO asymmetry by comparing the differences among these models as well as the differences between models and the observations.

An underestimate of the ENSO asymmetry is noted in all the models, but the latest version with the Neale and Richter scheme (CCSM3+NR) is getting closer to the observations than the earlier versions. The net surface heat flux is found to damp the asymmetry in the SST field in both models and observations, but the damping effect in the models is weaker than in observations, thus excluding a role of the surface heat flux in contributing to the weaker asymmetry in the SST anomalies associated with ENSO. Examining the subsurface signatures of ENSO—the thermocline depth and the associated subsurface temperature for the western and eastern Pacific—reveals the same

bias—the asymmetry in the models is weaker than in the observations.

The analysis of the corresponding AMIP runs in conjunction with the coupled runs suggests that the weaker asymmetry in the subsurface signatures in the models is related to the lack of asymmetry in the zonal wind stress over the central Pacific which is in turn due to a lack of sufficient asymmetry in deep convection (i.e., the nonlinear dependence of the deep convection on SST). In particular, the lack of westward shift in the deep convection in the models in response to a cold phase SST anomaly is found as a common factor that is responsible for the weak asymmetry in the models. We also suggest that a more eastward extension of the deep convection in response to a warm phase SST anomaly may also help to increase the asymmetry of ENSO. The better performance of CCSM3+NR is apparently linked to an enhanced convection over the eastern Pacific during the warm phase of ENSO. Apparently, either a westward shift of deep convection in response to a cold phase SST anomaly or an increase of convection over the eastern Pacific in response to a warm phase SST anomaly leads to an increase in the asymmetry of zonal wind stress and therefore an increase in the asymmetry of subsurface signal, favoring an increase in ENSO asymmetry.

1. Introduction

The El Niño-Southern Oscillation (ENSO) is one of the most important natural modes of the climate system and has been extensively studied (Philander 1990, Sun 2007). Two new dimensions of ENSO have emerged from the more recent investigation—the nonlinear and diabatic aspects of ENSO (Sun 2003, Sun et al. 2004, Sun and Zhang 2006). The sensitivity of ENSO to diabatic heating and its role as a basin-scale heat mixer in the tropical Pacific is linked to a critical quantity of ENSO—the asymmetry between its two phases, or as referred in some other studies, the residual of ENSO (Rodgers et al. 2004; Schopf and Burgman 2006). Relatedly, the ENSO asymmetry is potentially a mechanism for decadal variability (Rodgers et al. 2004; Sun and Yu 2009), and a cause of the bias in the time-mean background state (Sun and Zhang 2006; Schopf and Burgman 2006). The asymmetry between the two phases of ENSO was first noted in the SST fields, which manifest as the maximum warming during the warm phase exceeding the maximum cooling during the cold phase (or a positive skewness in the probability density distribution of the Niño3 SST anomaly) (Burgers and Stephenson 1999). Later the asymmetry has also been noted in the depth of the equatorial thermocline (Rodgers et al. 2004), in the upper ocean heat content (Tang and Hsieh 2003) and the subsurface temperature (Schopf and Burgman 2006, Sun and Zhang 2006).

The suggested physics mechanisms responsible for the asymmetry between El Niño and La Niña include the nonlinearity (or asymmetry) in the net surface heating or the upwelling cooling (Meinen and McPhaden 2000), the asymmetry of wind stress in the western and central tropical Pacific (Kang and Kug 2002), the nonlinear heating term in the surface heat budget equation (Jin et al. 2003), and a kinematic effect of oscillating a nonlinear temperature profile with finite-amplitude excursions that will cause the Eulerian time mean temperature to rise (fall) where the curvature of the temperature is positive (negative) as the amplitude of the oscillations increases (Schopf and Burgman 2006). In assessing the relationship between ENSO SST anomalies and the warm water volume (WWV), Meinen and McPhaden (2000) noted that for the same WWV anomaly, the corresponding warm El Niño SST anomaly is larger than the cold La Niña SST anomaly, and hence suggested that the relative importance of physical processes that control the growth of the warm and cold SST anomalies must be different. Specifically, they mentioned that the ENSO asymmetry may be caused by the asymmetry in the net surface heat flux into the ocean or the upwelling cooling. Although the net surface heat flux acts as a negative feedback that damps the growth of the ENSO SST anomaly in both phases, but may be more effective at heating the ocean during cold phases of ENSO than they are at cooling the ocean during warm phases of ENSO. Alternately, the ability of upwelling and vertical mixing to cool the surface may saturate at some threshold beyond which further thermocline shoaling does not lead to further SST cooling. By the use of National Centers for Environmental Prediction reanalysis data

and various ocean and atmosphere models, Kang and Kug (2002) suggested that the relatively weak SST anomalies during La Niña compared with those of El Niño are related to a westward shift of wind stress anomalies. They further attribute the westward shift of the windstress anomalies to the nonlinear dependence of deep convection on the SST which was noted earlier in Gadgil et al. (1984) and Hoerling et al. (1997). Jin et al. (2003) have suggested that nonlinear dynamical heating—the nonlinear term in the surface heat budget equation—may be a cause of the ENSO asymmetry. More recently, Schopf and Burgman (2006) demonstrated that oscillating a nonlinear temperature profile with finite-amplitude excursions can cause the Eulerian time mean temperature to rise (fall) where the curvature of the temperature is positive (negative) as the amplitude of the oscillations increases. This mechanism is found to be able to mimic observed changes in the mean sea surface temperatures in the Pacific between the 1920s, 1960s, and 1990s due to the changing ENSO amplitude.

After noting the positive skewness in the distribution of observed Niño3 SST anomalies, Burgers and Stephenson (1999) evaluated the ENSO asymmetry in the early NCAR Climate System Model (CSM1.0; Boville and Gent 1998) and found that the model underestimates the asymmetry in the Niño3 SST distribution. This bias in NCAR CSM1.0 was shown again by later studies that participated in the El Niño Simulation Intercomparison Project (ENSIP) (Hannachi et al. 2003) and the Coupled Model Intercomparison Project (CMIP) (An et al. 2005). Because NCAR CCSM1 (CSM1.0)

severely underestimates the amplitude of ENSO variability, Burgers and Stephenson (1999) suggested a link between the bias in the asymmetry and the bias in the amplitude. The simulation of the amplitude of ENSO variability—measured by the variance of Niño3 SST—in the late versions of NCAR CCSM is greatly improved (Deser et al. 2006). Does the improved simulation of the amplitude of ENSO variability also lead to a better simulation in the asymmetry of ENSO?

To answer this question, and more generally to explore the causes of the ENSO asymmetry, we will evaluate the ENSO asymmetry in five successive versions of the NCAR coupled models—NCAR CSM1 (Boville and Gent 1998), NCAR CCSM2 (Kiehl and Gent 2004), NCAR CCSM3 at T42, NCAR CCSM3 at T85 (Collins et al. 2006a), and NCAR CCSM3+NR (Neale et al. 2008). We will see that an improvement in simulating the variance of Niño3 SST does not guarantee an improvement in simulating the skewness.

Recognizing that the El Niño warming and La Niña cooling are driven by the vertical advection associated with subsurface temperature changes (Zebiak and Cane 1987), we will examine the asymmetry in the subsurface temperature. By examining the subsurface signal, we reasonably hope that we may obtain more information about the causes of bias in the simulated ENSO in CCSM, particularly in view of the findings by Sun and Zhang (2006) and Sun (2007). In these studies, they found that ENSO has a time mean effect on

the vertical temperature structure of the upper ocean—ENSO acts as a vertical heat mixer in the tropical Pacific. This time mean effect is apparently linked to the asymmetry between the upper ocean temperature anomalies during the two phases of ENSO. We will investigate the relationship between SST, convection, wind stress, and surface heat flux, particularly the asymmetry in these fields, attempting to discern and understand the mechanisms responsible for the asymmetry between the two phases of ENSO, and hence improve the processes involved that enable ENSO to have a "heat mixer" time-mean effect on the equatorial upper ocean temperature.

This paper is organized as follows. In Section 2, we introduce the methodology of our analysis and the models and observations used in the analysis. We present the assessment and analysis of ENSO asymmetry in the coupled NCAR models in Section 3. We will first assess the ENSO asymmetry in the SST (section 3.1) and then look at the asymmetry in upper ocean temperature in the models (section 3.2). We further analyze the corresponding fields of surface heat flux, precipitation, and surface wind stress (section 3.3). One thing that emerges from the analysis of these fields from the coupled models is an association between a weak asymmetry in the zonal wind stress and a weak asymmetry in the SST anomalies in the models. We present an analysis of the relationship between wind stress and SST in the corresponding AMIP runs of these coupled models (section 3.3), to demonstrate that the weak asymmetry in the zonal wind stress in the models is due to a less nonlinear dependence of deep convection on the

underlying SST in the models, and thereby underscore the role of this nonlinearity in giving rise to the asymmetry of ENSO. Summary and discussion are given in Section 4.

2. Methodology, data and model

To quantify the asymmetry of ENSO, we will examine the skewness of interannual variability of SST as well as the subsurface temperature of the equatorial upper Pacific. The skewness, $\sqrt{b_1}$ is defined as $\sqrt{b_1} = m_3/(m_2)^{3/2}$, where m_k is the k th moment, $m_k = (\sum_{i=1}^{N}(X_i - \overline{X})^k)/N$, and where X_i is the i th sample of variable X, $\overline{X}$ is the mean, and N is the number of samples (Burgers and Stephenson 1999). In addition to using skewness to measure the asymmetry of ENSO, we will do composites of El Niño, and La Niña, and then use the sum of the composite of these two phases of ENSO to measure the asymmetry.

Sustained climate modeling work through NCAR and its interaction with the climate community in the US and the world at large has made steady progress in building better and better climate system models. The effort has also created a suite of models with progressive changes, and offered a potential resource to address fundamental climate questions. Up till the writing of this paper, five major versions of NCAR models have been made available to the public. The five NCAR coupled models are NCAR CSM1 (Boville and Gent 1998), NCAR CCSM2 (Kiehl and Gent 2004),

NCAR CCSM3 at T42, NCAR CCSM3 at T85 (Collins et al. 2006a), and NCAR CCSM3+NR (Neale et al. 2008). We will examine the ENSO asymmetry in all these five versions and highlight the differences among these models and the progress made in simulating this particular aspect of ENSO.

The atmospheric component of CSM1, CCSM2, CCSM3 at T42, and CCSM3 at T85 is CCM3 (or CAM1) (Kiehl et al., 1998), CAM2 (Kiehl and Gent 2004), CAM3 at T42, and CAM3 at T85 (Collins et al. 2006b; Hack et al. 2006), respectively. From CCM3 (CAM1) to CAM2, there are several changes in physical parameterizations. First, the evaporation of convective precipitation back to the atmosphere was added in order to reduce the dry bias in the free troposphere in the model following Sundqvist (1988). Collins et al. (2002) also updated longwave radiation treatment of water vapor to enhance the longwave cooling in the upper troposphere. In addition, the RK treatment of stratiform clouds (Rasch and Kristjansson, 1998) was modified according to Zhang et al. (2003) that predicts the total (liquid+ice) cloud condensate (Boville et al. 2006; Zhang and Sun 2006). From CAM2 to CAM3, the physics of cloud and precipitation process has been modified extensively by Boville et al. (2006). The modifications include a) separate prognostic treatments of liquid and ice condensate, b) advection, detrainment, and sedimentation of cloud condensate, c) separate treatments of frozen and liquid precipitation, and d) the calculation of the cloud fraction. The radiation code has been updated with new parameterizations for the

longwave and shortwave interactions with water vapor (Collins et al. 2006a; Zhang and Sun 2006).

The ocean component of CSM1 is the NCAR CSM Ocean Model (NCOM) described in Gent et al. (1998). NCOM includes the mesoscale eddy parameterization of Gent and McWilliams (1990), and the vertical mixing scheme based on the *K*-profile parameterization scheme of Large et al. (1994). The ocean component of CCSM2 uses the Parallel Ocean Program code developed at the Los Alamos National Laboratory (Smith et al. 1992). The mesoscale eddy parameterization and the vertical mixing scheme are the same as those used in the ocean component of CSM1. The ocean component of CCSM3 is based upon the Parallel Ocean Program version 1.4.3 (POP; Smith and Gent 2002). The CCSM3 ocean model has two important improvements over CCSM2 as discussed by Danabasoglu et al. (2006). These are modifications to the Large et al. (1994) *K*-profile parameterization and implementation of spatially varying monthly solar absorption based on ocean color observations.

CCM3 (CAM1), CAM2, and CAM3 share the same convection scheme, however. The deep convection is parameterized following Zhang and McFarlane (1995). Shallow convection is parameterized according to Hack (1994).

CCSM3+NR is a developing version based on its immediate predecessor, CCSM3 (Neale et al. 2008). It uses a modified deep convection scheme—Neale and Richter

convection scheme to replace the Zhang and McFarlane deep convection scheme (Zhang and McFarlane 1995) used in CCSM3. The changes to the existing parameterization of deep convection (Zhang and McFarlane 1995) are the inclusion of Convective Momentum Transports (CMT) and a dilution approximation for the calculation of Convective Available Potential Energy (CAPE) (Neale et al. 2008).

The observational SST data for our evaluation are from the Hadley Centre Sea Ice and SST (HadISST) dataset (Rayner et al. 2003). The surface heat flux data are from the European Centre for Medium-Range Weather Forecasts (ECMWF) reanalyses ERA-40 (Uppala et al., 2005). The wind stress data are obtained from the simple ocean data assimilation (SODA) set (Carton and Giese 2008) in which the surface winds are a combination of ERA-40 reanalysis and QuikSCAT satellite observations. Observations of precipitation are obtained from the CPC Merged Analysis of Precipitation (CMAP) (Xie and Arkin, 1997). The simple ocean data assimilation (SODA) set (Carton et al. 2000) is used for validating the upper ocean temperature in the models.

3. Results

3.1 Asymmetry in the SST fields

Figure 1 shows histograms of the distribution of Niño-3 SST anomalies for observations (1950-1999) and five NCAR coupled models. The histogram from the

observations has a longer tail on the right. The maximum positive anomaly in the observations is close to 3.5^{o}C while the maximum negative anomaly is limited to -2.5^{o}C. This skewness towards warm El Niño events has been noted by previous studies (e.g., Burgers and Stephenson 1999 and others). The models, however, clearly have a more Gaussian-like distribution. There are progressive increases in the range of variability from CCSM1 to CCSM3+NR. The range of the variability of Niño-3 SST in the latest version has in fact become very comparable to the observations. The frequency distribution of the anomalies in the latest version is more spread out within the range confined by the maximum positive and negative anomalies, compared to that in four old versions. In other words, there are relatively few instances with weak anomalies in the latest version. The overall distribution for Niño-3 anomalies is much closer to normal distribution in the NCAR models than in observations. A positive skewness is evident in the histogram for the latest version, however.

Table 1 lists the skewness of Niño-3 SST anomalies from observations and the models together with their variance. The observed skewness value of 0.86 is the same as that obtained by Burgers and Stephenson (1999). The standard deviation in the present study (0.88 ^{o}C) is slightly smaller than the findings of Burgers and Stephenson (1999) (0.91 ^{o}C). The possible reason is that HadISST data may underestimate the SST variability before 1981 due to the EOF filters used for interpolation. The numbers in the table confirm the impression from the histograms that the models underestimate the skewness of Niño-3 SST anomalies. Among the five models, the latest CCSM3+NR has

the strongest ENSO variability and a significant positive skewness. It is interesting to note that there is a much weaker ENSO variability in CCSM1, but the skewness in CCSM1 is comparable to that in CCSM3+NR. On the other hand, the variance of ENSO in CCSM2 and CCSM3 is quite comparable to the observed, but these two models almost have not skewness at all. So an increase in the variance of Niño3 SST anomalies does not necessarily lead to an increase in the skewness. A related question raised by the results in Table 1 is that the variance alone may not be a good indicator for the actual level of ENSO activity in the models. For example, measured by the variance of Niño-3 SST anomalies alone, one would conclude that the level of ENSO variability in CCSM2, CCSM3, and CCSM3 at T85 is comparable to observations, but quantifying the skewness of Niño-3 SST anomalies in these models indicates otherwise.

To get another measure of ENSO asymmetry, we construct composites of El Niño and La Niña events. Figure 2 gives the spatial pattern of composite SST anomalies during El Niño and La Niña events from observations and five NCAR models. In observations, the positive SST anomalies associated with warm events tend to extend more to the South American coast compared to the negative anomalies associated with cold events. This feature is not evident in the models. Both the El Niño and La Niña composites in observations have a wider meridional extension of the SST anomalies than in four earlier versions of NCAR models (CCSM1, CCSM2, and two CCSM3 models). Positive SST anomalies associated with El Niño and negative SST anomalies associated

with La Niña in these models also extend too far westward, consistent with the existence of an excessive cold-tongue in these models (Sun et al. 2006). The latest CCSM3+NR has an improvement in the zonal and meridional extension of the SST anomalies and this has been noted already by Neale et al. (2008). The observed maximum SST anomaly of 1.6 ^{o}C around 110^{o}W is well captured in CCSM3+NR during the warm phase, while the negative SST anomaly is somewhat overestimated in the model during the cold phase.

The spatial distribution of the asymmetry between El Niño and La Niña events is shown in Figure 3. The asymmetry pattern is defined as the sum of El Niño and La Niña composites. In observations, the asymmetry map has a similar spatial structure of the El Niño events (Fig. 3a). The figure is characterized by positive SST anomalies of about 0.2-0.5^{o}C over the central and eastern tropical Pacific and small negative anomalies of about -0.1^{o}C over the western tropical Pacific. The main bias in the models is a severe underestimate of positive anomalies over the eastern tropical Pacific (Figures 3b-3f). The skewness pattern (contour of right panel) is very similar to the pattern of sum of warm and cold events (left panel) and indicates again an underestimate of positive skewness over the eastern tropical Pacific in the models. It appears that there is hardly any SST asymmetry in four previous versions. By comparison, the latest CCSM3+NR shows a significant improvement, but the skewness in the model does not even reach half of the observed value in the eastern Pacific, and

has a stronger negative skewness in the western Pacific. We have also noted that over the central Pacific, the cold bias in SST climatology (shaded) in the NCAR CCSM1 and CCSM2 is accompanied with a positive skewness opposite to the observed (Figures 3h, 3i). As remarked by Meinen and McPhaden (2000), in the upwelling zone, the depth of the thermocline is more bounded on its lower side than its upper side—the depth can be shallower if it already reaches the surface. This asymmetry would favor a positive skewness in the SST anomaly. This reasoning also suggests that a cold-bias in the mean SST in the central Pacific due to a shallower thermocline should contribute to a positive bias in the skewnss, which is apparently what we see here. The warm bias in SST climatology (shaded) in the western Pacific, on the other hand, is accompanied with a stronger negative skewness (Figures 3j, 3l). This is probably due to the sensitivity of deep convection to the total SST, since the upwelling is very weak over these regions. Deep convection tends to occur only when the total SST is sufficiently high. Through the albedo of its anvils and the efficient horizontal heat dispersion in the tropics, deep convection has been shown to damp the growth of a warm SST anomaly (Ramanathan and Collins 1991, Wallace 1992, and Sun and Trenberth 1998).

3.2 Asymmetry in the subsurface temperature

Next we will look at the asymmetry of subsurface signal. As demonstrated in the pioneering studies of ENSO (Zebiak and Cane 1987 and others), the SST anomaly in

the eastern Pacific associated ENSO is driven by the subsurface temperature anomaly in that region which is in turn related to the subsurface temperature anomaly in the western Pacific. Figure 4 shows the equatorial upper ocean temperature anomalies during both phases of ENSO. Observations show a maximum positive anomaly of 2.5 ^{o}C during warm phase in the eastern Pacific (Fig. 4a) and a maximum negative anomaly of -1.5^{o}C during cold phase in the eastern Pacific (Fig.4g). The location of the maximum response occurs approximately in the region of 120^{o}W to the eastern coast at a depth about 50-100 m. During the warm phase, four old versions of CCSM have a much weaker positive subsurface temperature anomaly over the eastern Pacific. The underestimate of the anomaly ranges from about 2 ^{o}C in CCSM1 to 1 ^{o}C in CCSM3. The positive anomalies in the models are more confined to the surface and extend too far to the west. These anomalies in the mixed layer appear to be caused by processes associated with changes in upwelling, heat flux, and vertical mixing over most regions. The accompanying negative temperature anomalies in the subsurface of the western Pacific are also underestimated in these models. The maximum negative temperature anomaly occurs at about the same depth as that in the observations, but is more eastward. The axis of maximum negative temperature anomaly in the depth-longitude plane is more horizontal in the models than in the observations. In terms of magnitude, the upper ocean temperature anomalies in the latest version CCSM3+NR is comparable to those in observations.

During the cold phase, the models do a better job in simulating the upper ocean temperature anomalies than in the warm phase. The negative temperature anomalies in CCSM1 and CCSM2 are underestimated, but those in two versions of CCSM3 are comparable to the observed over the eastern Pacific. The latest version CCSM3+NR has stronger subsurface temperature anomalies than in the observations. CCSM3+NR differs from the observed value in its simulation of the subsurface temperature anomaly over the western Pacific by as much as 0.25 ^{o}C. Again, we noted that over the western Pacific the shape of subsurface temperature anomalies in observations differs from those in the models—the former have a more downward tilt from the west to the east while the latter are more horizontal.

Fig. 5 shows the time-mean thermocline depth (indicated by 20 ^{o}C isotherm depth) in observations and models. The observed thermocline depth over the western Pacific increases from 150 m to around 175 m, showing a downward tilt from the west to the east. The modeled thermocline depth is either flat or has slightly upward tilt from the west to the east in the western Pacific. In terms of zonal extent, there is a progressive increase in the size of the western Pacific warm-pool.

Figure 6 shows a basin-wide view of the thermocline depth anomalies during the warm and cold phases. All the models except CCSM1 can simulate the observed feature: the thermocline depth is increased in the tropical eastern Pacific and decreased in the

central and western Pacific during the warm phase, and a reversed situation occurs during the cold phase. The magnitude of the thermocline depth anomalies, however, is underestimated in the models especially over the eastern Pacific during the warm phase. This may contribute to the small subsurface temperature anomalies in most models during the warm phase. By comparison, CCSM3+NR has a close pattern to the observed because of an improvement in the meridional extension.

To examine the subsurface signatures of ENSO asymmetry, we add the upper ocean temperature anomalies over the two phases. We do the same sum for the depth of thermocline. Figure 7 shows the results—the left panels show the asymmetry in the upper ocean temperature anomalies and the right panels show the asymmetry in the thermocline depth anomalies. Observations indicate a positive asymmetry of subsurface temperature of 1 ^{o}C around 75-m depth over the eastern Pacific, and a negative asymmetry of 0.4 ^{o}C in subsurface temperature in the western Pacific. All the models underestimate the asymmetry in subsurface temperature. Therefore the weaker SST asymmetry in the models is likely associated with an underestimate of the asymmetry in subsurface temperature. Again, CCSM3+NR has an increased positive asymmetry in subsurface temperature compared to other old versions (Fig.7f). We have calculated the sum of warm and cold anomalies for the upper ocean heat content (defined as the ocean temperature averaged over the upper 260 meters). The asymmetry pattern of ocean heat content is very similar to that of SST shown in the left panel of Figure 3 (not shown).

There is hardly any asymmetry of ocean heat content over the eastern Pacific in the four earlier versions, while the improvement is evident in CCSM3+NR. The underestimate of the asymmetry in the subsurface temperature anomalies also shows up in the asymmetry in the depth of thermocline (right panel of Fig.7). The asymmetry in the observed thermocline depth anomalies is characterized by a broad negative region in the western Pacific. This feature is largely absent in the four earlier versions of the model. The latest version of the model has a negative asymmetry in the western Pacific, but the negative asymmetry is still too confined to the equator, and the maximum is located too far to the east.

Fig. 8 further shows the meridional structures of the asymmetry in the upper ocean temperature anomalies over the western Pacific and eastern Pacific. Observations are characterized by two maximum values of negative asymmetry off the equator in both hemispheres over the western Pacific (Fig.8a) and a strong positive asymmetry right at the equator over the eastern Pacific (Fig.8g). The negative asymmetry over the western Pacific covers a wider meridional region extending from 10 ^{o}S to 10 ^{o}N while the positive asymmetry over the eastern Pacific is mainly confined within the equator (5 ^{o}S-5 ^{o}N). These negative and positive anomalies appear to be associated with the equatorial Rossby and Kelvin waves, respectively. Except for a better simulation of the negative asymmetry over the region of 5 ^{o}N-10 ^{o}N in the western Pacific in CCSM3 (Fig.8d), all the models underestimate the negative asymmetry over the western Pacific and the positive asymmetry over the eastern Pacific. The improvement of the

asymmetry in the meridional sections over the eastern Pacific in the new version CCSM3+NR is not as obvious as that in the zonal cross sections noted earlier (Fig.8l). This is expected because of the cancellation between the positive asymmetry over the far eastern Pacific and the overly negative asymmetry over the region of 150 ^{o}W-120 ^{o}W as shown in Fig.7f.

To obtain a qualitative measure of the asymmetry in the subsurface temperature, we plot the histogram of the monthly mean Niño-3 subsurface temperature anomalies (Figure 9). The figure shows that the observed Niño-3 subsurface temperature anomalies are skewed to the positive values and the maximum positive anomalies can reach more than 6 ^{o}C. The underestimate of the maximum positive anomalies in the models ranges from 5 ^{o}C in CCSM1 to 2 ^{o}C in CCSM3+NR. Although the overall distribution in the models is close to normal distribution, the new version CCSM3+NR has a more similar shape to the observed among five models.

The skewness and variance of the subsurface temperature anomalies are further shown in Table 2. The results confirm that all the models underestimate the variability and skewness of Niño-3 subsurface temperature. Comparing Table 2 with Table 1 indicates that the interannual variability of Niño-3 subsurface temperature is almost as twice strong as that of Niño-3 SST in observations. But the contrast in the strength of variability between the surface and the subsurface in the models is not as significant as the observed. In fact, the subsurface temperature variability is even weaker than SST

variability in two old versions (CCSM1 and CCSM2). Table 2 also shows that in the models, there are a good correspondence between the weaker variability of subsurface temperature and the underestimate of the skewness of subsurface temperature over the Niño-3 region. From Table 2, we find that over the western Pacific the observed negative asymmetry of subsurface temperature (Tsub_WP) is underestimated in all the models, which is consistent with the results shown in the left panel of Figure 7. Further considering the underestimate of the positive asymmetry in Niño-3 subsurface temperature (Tsub_Nino3), we are not surprised at the findings that the underestimate of the positive asymmetry in the difference of subsurface temperature between Niño-3 region and western Pacific (Tsub_diff) is more severe in all the models, accompanied with an enhanced underestimate of the variability of subsurface temperature in most models (the underestimate of Tsub_diff variability in CCSM3+NR is not as much as that of Tsub_Nino3 variability due to an increase of Tsub_WP variability in this model). Stronger SST variability does not necessarily result in a stronger SST skewness. For example, we note that CCSM2 and CCSM3+NR have a larger SST variability than observations but have a weaker skewness of SST. CCSM1 has a much weaker SST variability than CCSM2 but the skewness value in the former is much larger than that in the latter (Table 1). But in the subsurface (Table 2), the models with smaller variance of subsurface temperature have a smaller skewness value and those with larger variance have a relatively larger skewness value over the Niño-3 region. It is thus suggested that the subsurface temperature anomalies may be a good proxy as a measure of the

relationship between ENSO variability and asymmetry, since there seems to be no correlation between SST variance and SST skewness. Clearly, the present findings reveal that the lack of the asymmetry in SST field in the NCAR models is linked to an underestimate of the asymmetry in subsurface temperature.

3.3 Possible causes for the weak ENSO asymmetry in the models

A. Role of Surface Heat Flux

Figure 10 shows the composite of the net surface heat fluxes for the two phases of ENSO. The figures show that four earlier versions of the NCAR model underestimate the negative heat flux anomalies during the warm phase. These models also underestimate the positive anomalies during the cold phase. The underestimate of surface heat flux anomalies in four earlier versions is mainly caused by an underestimate of the negative anomalies of net surface shortwave flux during the warm phase and an underestimate of the positive anomalies of net surface shortwave flux during the cold phase. The contribution from the bias in the latent heat flux anomalies is relatively small (not shown). Regression of the surface heat flux onto the SST further reveals that the four earlier versions of the model underestimate the damping effect of the net surface heat flux on the local SST—the slope of the surface heat flux against the SST in these models is much weaker than that in observations especially for the slope against positive SST anomalies (Figure 11). The difference between the slope against positive SST anomalies and that against negative SST anomalies in the four earlier

versions is also much smaller than that in observations, indicating a less nonlinear relationship between surface heat flux and SST in these models. The surface heat flux-SST relationship is much improved in CCSM3+NR (-18.4 $Wm^{-2}K^{-1}$ in the model versus the observed -21.5 $Wm^{-2}K^{-1}$ for positive SST anomalies, and -9.3 $Wm^{-2}K^{-1}$ in the model versus the observed -12.9 $Wm^{-2}K^{-1}$ for negative SST anomalies). The increase of net surface shortwave flux anomalies during two phases of ENSO is responsible for the improvement of surface heat flux anomalies in the new version. The new model also has an improved asymmetry pattern in the surface heat flux although the magnitude of asymmetry is underestimated over the central and eastern Pacific (by 10~15 Wm^{-2}) (Figure 11l) due to an overestimate of positive anomalies of net surface shortwave flux during the cold phase. The match of the stronger positive asymmetry of heat flux over the western Pacific (Figure 11l) with the stronger negative asymmetry of SST over that region (Figures 3f and 3l) indicates a good negative correlation between the asymmetry of surface heat flux and the asymmetry of SST in the new model. It is clear that all the NCAR models underestimate the damping effect of surface heat flux on SST over the central and eastern Pacific (right panel of Fig.11). Thus the underestimate of the ENSO asymmetry is not likely due to the contribution from the surface heat flux.

B. Role of Surface Winds

The precipitation anomalies during the warm and cold phases are shown in Figure 12. Observations show that the maximum of precipitation anomalies during the warm phase

locates at about 180^{o} with the magnitude of 4 mm day^{-1} whereas the maximum of precipitation anomalies during the cold phase shifts westwards and centers at 170^{o}E with the magnitude of -3 mm day^{-1}. Such a shift is less obvious in the models. A weaker response in the precipitation during the warm phase over the equatorial central and eastern Pacific is evident in four old versions, but one can see the progressive improvement in these models in the location of the center of response as well as the magnitude of the response of the precipitation. The center of maximum precipitation in CCSM3+NR is even more eastward than in the observations. The precipitation anomalies during the warm phase of ENSO over the eastern Pacific in this latest version are more comparable to that in the observations, although the maximum precipitation response in this new model is still somewhat weaker than the observations. CCSM3+NR also starts to get the negative anomalies in the western Pacific, a feature that is almost entirely missing in four old versions in the western Pacific.

The negative precipitation anomalies during the cold phase in the models (CCSM1, CCSM2, and CCSM3 at T42) are generally weaker than in the observations in the central Pacific. In the central Pacific, the negative precipitation anomalies in CCSM3+NR are comparable to the observations. The precipitation anomaly in the far eastern Pacific in this latest version is even stronger than in the observations, consistent with the stronger negative SST anomalies over that region (Fig.2l). A common bias in all these models is the lack of the positive precipitation anomalies in the western Pacific. Another common bias is a double rain-band in the eastern Pacific, which exists in the

warm phase as well, particularly for CCSM2, CCSM3 (T42), and CCSM3 (T85).

The associated zonal wind stress anomalies during the warm and cold phases are shown in Figure 13. Observations show that the center of equatorial zonal wind anomalies locates at about 170^{o}W during the warm phase and at 180^{o} during the cold phase. The westward shift of the center of zonal wind anomalies during the cold phase relative to the warm phase is consistent with the shift in the observed precipitation anomalies. During the warm phase, the positive zonal wind stress anomalies are more confined within 5^{o}S-5^{o}N and the magnitude is underestimated in four old versions. But the progressive improvement is again evident. In contrast to the four earlier versions, CCSM3+NR is distinctly closer to the observations. It not only has an improvement in simulating the meridional extension of zonal wind stress anomalies, but also has an improvement in simulating the magnitude of zonal wind stress anomalies. However, the center of maximum wind stress anomaly is shifted eastward by about 10~20^{o} in all the models during the warm phase (left panel of Fig.13). During the cold phase the negative anomalies of zonal wind stress are still more confined to the equatorial region of 5^{o}S-5^{o}N in the old models. CCSM3+NR better captures the pattern of negative anomalies (right panel of Fig. 13). Again, the eastward shift of the center of zonal wind stress anomalies is evident in all the models relative to observations during the cold phase. Compared to four old versions, CCSM3+NR has a wider zonal extension of stronger negative wind stress anomalies, ranging from 170^{o}E to 140^{o}W (Fig.13l), which

is associated with a wider zonal distribution of negative precipitation anomalies during the cold phase (Fig.12l). The stronger negative zonal wind stress anomaly in CCSM3+NR is also consistent with a stronger negative SST anomaly during the cold phase (Fig.2l).

The sum between warm composite anomalies and cold composite anomalies in precipitation and zonal wind stress is shown in Figure 14. Observations show a strong asymmetry in precipitation fields—a strong positive asymmetry in the central and eastern Pacific and a strong negative asymmetry in the western Pacific (Figure 14a). With the exception of the CCSM3+NR, such an asymmetry does not exist in the models. The underestimate of the asymmetry in the precipitation anomalies in four old versions (Figures 14b-14e) is due to the lack of convection in the warm phase (Figures 12b-12e). An increase of precipitation in the warm phase over the central and eastern Pacific in the latest CCSM3+NR improves the asymmetry of precipitation (Figure 14f).

Consistent with the weak asymmetry in precipitation anomalies, the asymmetry in zonal wind stress anomalies is also weak in the NCAR models (right panel of Figure 14). Again, the new version CCSM3+NR has an improved asymmetry pattern of zonal wind stress anomalies because of the improvement in simulating the asymmetry in the precipitation anomalies (Figures 14f and 14l).

The above analysis of the precipitation and zonal wind stress fields links the weak

asymmetry in the latter in the models to the weak asymmetry in the former. Is the weak asymmetry in these two fields a consequence of the weak asymmetry in the corresponding SST fields or the cause of the latter? To answer this question, we have further analyzed the precipitation and zonal wind stress from the corresponding AMIP runs. Figure 15 gives the asymmetry pattern of precipitation and zonal wind stress from the corresponding AMIP runs of the NCAR models—runs that are forced by the observed SST boundary conditions and therefore have identical SST patterns to those in observations. Although the SSTs now are the same as the observed, the asymmetry in precipitation over the eastern Pacific in three old versions (CCM3, CAM2, and T42 CAM3) is notably weaker. The positive asymmetry in precipitation in T85 CAM3 and CAM3+NR in the central and eastern equatorial Pacific is more comparable to the observations, but the corresponding negative asymmetry in the western Pacific (140^{o}E-170^{o}E) is weaker than what is seen in the observations. In fact, all the models underestimate the negative asymmetry in the precipitation response to ENSO forcing over the equatorial western Pacific (140^{o}E-170^{o}E, 5^{o}S-5^{o}N), and the underestimate of negative asymmetry ranges from 1.0 mm/day in T85 CAM3 to 1.7 mm/day in CAM2 (left panel of Figure 15). This underestimate of the negative asymmetry over the western Pacific is mostly due to an underestimate of the drying during the cold phase in that region for all the models except CCM3 (Fig. 16). The negative anomalies of precipitation in CCM3 over the equatorial western Pacific (140^{o}E-170^{o}E, 5^{o}S-5^{o}N) are close to the observed during the cold phase (-1.2 mm/day in the model versus the

observed -1.3 mm/day), but during the warm phase the underestimate of negative anomalies is large (0.6 mm/day in the model versus the observed -0.4 mm/day) due to an overly westward extension of the positive anomalies in this model (Fig.16b), resulting in the weaker negative asymmetry over the equatorial western Pacific shown in Fig. 15b. For the other four models, the underestimate of the negative anomalies over the equatorial western Pacific is small during the warm phase (ranging from 0.3 mm/day in CAM2 to 0.4 mm/day in CAM3). By comparison, the underestimate of the negative anomalies over the equatorial western Pacific is large during the cold phase (ranging from 0.7 mm/day in T85 CAM3 to 1.4 mm/day in CAM2). This bias is related to a lack of a significant westward shift of the location of the maximum response of precipitation from the warm phase to the cold phase. The response of precipitation to ENSO SST forcing in the models is apparently too local. This lack of spatial shift in the precipitation response is apparently also the cause of the positive weak asymmetry in the central and eastern Pacific (The models can capture the observed asymmetry in the magnitude response between the two phases: the maximum response during the warm phase is greater than the maximum response during the cold phase). With the exception of CAM3+NR, the precipitation response in the eastern Pacific during the warm phase is too weak.

Consistent with the lack of the westward shift in the pattern of precipitation response, there is also lack of shift in the models in the pattern of zonal wind stress (Fig. 17). This

bias is apparently the main cause of the substantially weak negative zonal wind stress asymmetry in the equatorial western Pacific in all the models, and the weak positive zonal wind stress asymmetry in the central and eastern Pacific in CCM3, CAM2, and CAM3-T42 (see the right panel of Figure 15). Despite of the lack of the spatial shift between the two phases of ENSO, the positive asymmetry in the central and eastern equatorial Pacific in CAM3-T85 and in CAM3+NR is more comparable to observations. This is because the asymmetry in the magnitude response in these two models is actually greater than that in the observations. Measured by the maximum response in the central equatorial Pacific, the asymmetry in the magnitude in observations is about 6 $X10^{-3}N/m^2$. This asymmetry in maximum magnitude in the latest two models reaches more than 9 $X10^{-3}N/m^2$ and 9 $X10^{-3}N/m^2$ respectively primarily because of the much stronger zonal wind stress response in the warm phase (Figure 17). A close examination of the difference between these two later models reveals that the zonal wind stress response during the warm phase extends more eastward in CAM3+NR. Correspondingly, during the warm phase the negative response of the zonal wind stress over the far eastern equatorial Pacific in the latest version is also weaker: moving towards the observed (Figure 17f). These differences are apparently linked to the difference in the precipitation response to the SST forcing in these two models, because the precipitation response in the eastern Pacific (150^oW-80^oW) is stronger in CAM3+NR than in CAM3-T85 and therefore closer to the observed during the warm phase (Figs. 16a, e and f).

Overall, the results from the AMIP runs suggest that the weak asymmetry in the SST is likely due to a weaker asymmetry in the precipitation response to the SST forcing. In the observations, there is a significant westward shift in the maximum response in the precipitation from the warm phase to the cold phase. But models do not simulate this shift. With the exception of the latest version, the precipitation response in the eastern Pacific during the warm phase also tends to be too weak. These biases are then reflected in the zonal wind stress: a weaker asymmetry in the zonal wind stress. Such a bias is then reinforced in the coupled models as the resulting weaker asymmetry in the zonal wind stress causes a weaker asymmetry in the SST through the subsurface dynamics (see Figures 4 and 7). The latter then in turn generates an even weaker asymmetry in the precipitation and thereby an even weaker asymmetry in the zonal wind stress.

4. Summary

In this study, we have evaluated the ENSO asymmetry in five successive versions of Community Climate System Models (CCSMs). We find that all the versions underestimate the ENSO asymmetry. This underestimate is found in both the SST and the subsurface temperature signatures of ENSO. We also find that the net surface heat flux damps the ENSO asymmetry in the SST field and the models underestimate this damping effect. In light of the results from the corresponding AMIP runs, we suggest

that the lack of asymmetry in the SST field of ENSO is due to the weaker asymmetry in the precipitation response in the models than in the observations to a given SST forcing. In particular, we attribute the weaker asymmetry to the lack of westward shift in the precipitation response from the warm phase to the cold phase in the models. The weaker asymmetry in the precipitation then causes a weaker asymmetry in the zonal wind stress response. In the process of coupling, this bias is then introduced to the subsurface through the wind forcing, and then to the SST response. The positive loop between the SST, precipitation, and zonal wind stress then reinforces the bias, causing a substantial underestimate of the asymmetry of ENSO in the coupled models.

It has long been known that the dependence of deep convection on the SST is nonlinear (e.g., Graham and Barnett 1987). The response of precipitation to a change in the sign of an anomalous SST forcing in the central and eastern Pacific is consequently asymmetric (This nonlinearity is fundamentally related to the existence of the zonal SST gradient in the mean state). An asymmetric response in the precipitation then causes an asymmetric response in the zonal wind stress (Hoerling et al. 1997; Kang and Kug 2002). Our study therefore underscores the importance of simulating accurately the nonlinear dependence of deep convection on the SST in climate models.

The evaluation also reveals that models with stronger variance in the Niño-3 SST than observations do not necessarily have a stronger SST skewness. By examining the

nonlinearity in the Niño-3 SST time series from 24 coupled models participating in the El Niño Simulation Intercomparison Project (ENSIP), Hannachi et al. (2003) also found that some models have larger variance but have small SST skewness value (see their Table 4). To the extent that the phase asymmetry is a fundamental feature of the observed ENSO, using the Niño-3 SST variance alone to measure the level of ENSO activity in the models can be misleading.

Among five NCAR models, the latest CCSM3+NR has the best simulation of the ENSO asymmetry, although the asymmetry is still substantially weak than in the observations. This improvement appears to be a consequence of a stronger and broader response of precipitation (and zonal wind stress) to SST forcing during the warm phase of ENSO, which improves the asymmetry in the central Pacific in the response of precipitation to ENSO SST forcing and thereby in the response of zonal wind stress to ENSO SST forcing. The stronger asymmetry in the zonal wind stress then helps to create a stronger asymmetry in the subsurface temperature, which in turn contributes to a stronger asymmetry in the SST. Contrasting with earlier versions of the NCAR CCSM suggests that the increase in deep convection over the central and eastern Pacific during the warm phase in the latest CCSM3+NR is a consequence of the replacement of Zhang and McFarlane deep convection scheme (Zhang and McFarlane 1995) by the Neale and Richter convection scheme (Neale et al. 2008).

The ENSO asymmetry over the eastern Pacific in CCSM3+NR is still weaker than that in observations. In light of the results from the AMIP runs, the reason appears to be that although the positive response in the precipitation asymmetry over the central and eastern Pacific to ENSO forcing is adequately strong, a significant negative response in the precipitation asymmetry to ENSO forcing over the equatorial western Pacific is still missing due to the lack of a westward shift of convection during the cold phase. To improve the spatial shift in the location of deep convection in the models in response to ENSO forcing appears to be a key step to take to further improve the simulation of ENSO—its asymmetry in particular.

Acknowledgement

This research was supported by NOAA's Climate Dynamics and Environmental Prediction Program, and by NSF's Climate Dynamics Program under ATM-9912434, ATM-0331760, and ATM 0553111. The leading author would like to thank Jon K. Eischeid for providing the *t*-test code.

References

An, S.-I., Y.-G. Ham, J.-S. Kug, F.-F. Jin, and I.-S. Kang, 2005: El Niño–La Niña Asymmetry in the Coupled Model Intercomparison Project Simulations. *J. Climate*, **18**, 2617–2627.

Boville B. A., and P. R. Gent, 1998: The NCAR Climate System Model, version one. *J. Climate*, **11**, 1115–1130.

Boville, B. A., P. J. Rasch, J. J. Hack, and J. R. McCaa, 2006: Representation of clouds and precipitation processes in the Community Atmosphere Model (CAM3). *J. Climate*, **19**, 2184–2198.

Burgers G., and D. B. Stephenson, 1999: The "normality" of El Nino. *Geophys. Res. Lett.*, **26**, 1027–1030.

Carton J., G. Chepurin, X. Cao, and B. Giese, 2000: A simple ocean data assimilation analysis of the global upper ocean 1950–95. Part I: Methodology. *J. Phys. Oceanogr,* 30, 294–309.

Carton J. A., and B. S. Giese, 2008: A reanalysis of ocean climate using Simple Ocean Data Assimilation (SODA). *Mon. Wea. Rev*., 136, 2999–3017.

Collins, W. D., J. K. Hackney, and D. P. Edwards, 2002: An updated parameterization for infrared emission and absorption by water vapor in the National Center for Atmospheric Research Community Atmosphere Model. *J. Geophys. Res.,* 107(D22), 4664, doi:10.1029/2001JD001365.

Collins W. D., Coauthors, 2006a: The Community Climate System Model version 3

(CCSM3). *J. Climate*, **19**, 2122–2143.

Collins, W. D., P. J. Rasch, B. A. Boville, J. J. Hack, J. R. McCaa, D. L. Williamson, B. P. Briegleb, C. M. Bitz, S.-J. Lin, and M. H. Zhang, 2006b: The formulation and atmospheric simulation of the Community Atmosphere Model version 3 (CAM3), *J. Climate*, **19**, 2144–2161.

Danabasoglu G., W. G. Large, J. J. Tribbia, P. R. Gent, B. P. Briegleb, and J. C. McWilliams, 2006: Diurnal coupling in the tropical oceans of CCSM3. *J. Climate*, **19**, 2347–2365.

Deser, C., A. Capotondi, R. Saravanan, and A. S. Phillips, 2006: Tropical Pacific and Atlantic Climate Variability in CCSM3. *J. Climate*, **19,** 2451–2481.

Gadgil, S., P. V. Joseph, and N. V. Joshi, 1984: Ocean–atmosphere coupling over monsoon regions. *Nature*, **312**, 141–143.

Graham, N. E., and T. P. Barnett, 1987: Sea Surface Temperature, Surface wind divergence, and convection over tropical oceans. *Science*, **238,** 657 – 659.

Gent, P. R., F. O. Bryan, G. Danabasoglu, S. C. Doney, W. R. Holland, W. G. Large, and J. C. McWilliams, 1998: The NCAR Climate System Model global ocean component. *J. Climate*, **11**, 1287–1306.

Gent, P. R., and J. C. McWilliams, 1990: Isopycnal mixing in ocean circulation models. *J. Phys. Oceanogr.,* **20**, 150–155.

Hack, J. J., 1994: Parameterization of moist convection in the National Center for Atmospheric Research Community Climate Model (CCM2). *J. Geophys. Res.,* **99**,

5551–5568.

Hack, J. J., J. M. Caron, G. Danabasoglu, K. W. Oleson, C. M. Bitz, and J. E. Truesdale, 2006: CCSM-CAM3 climate simulation sensitivity to changes in horizontal resolution. *J. Climate*, **19**, 2267–2289.

Hannachi A., D. Stephenson, and K. Sperber, 2003: Probablity-based methods for quantifying nonlineararity in the ENSO. *Climate Dyn.*, **20**, 241–256.

Hoerling, M. P., A. Kumar, and M. Zhong, 1997: El Niño, La Niña, and the nonlinearity of their teleconnections. J. Climate, **10**, 1769–1786**.**

Jin F.-F., S.-I. An, A. Timmermann, and J. Zhao, 2003: Strong El Niño events and nonlinear dynamical heating. *Geophys. Res. Lett.*, **30**, 1120, doi:10.1029/2002GL016356.

Kalnay, E., et al., 1996: The NCEP/NCAR 40-year reanalysis project, Bull. Am. Meteorol. Soc., 77, 437–471.

Kang I.-S., and J.-S. Kug, 2002: El Niño and La Niña sea surface temperature anomalies: Asymmetry characteristics associated with their wind stress anomalies. *J. Geophys. Res.*, **107**, 4372, doi:10.1029/2001JD000393.

Kiehl, J. T., J. J. Hack, G. Bonan, B. A. Boville, D. Williamson, and P. J. Rasch, 1998, The National Center for Atmospheric Research Community Climate Model: CCM3, *J. Climate*, **11**, 1131–1149.

Kiehl J., and P. Gent, 2004: The Community Climate System Model, version 2. *J. Climate*, **17**, 3666–3682.

Large W. G., J. C. McWilliams, and S. C. Doney, 1994: Oceanic vertical mixing: A review and a model with a nonlocal boundary layer parameterization. *Rev. Geophys,* **32**, 363–403.

Meinen, C. S., and M. J. McPhaden, 2000: Observations of warm water volume changes in the equatorial Pacific and their relationship to El Niño and La Niña. *J. Climate*, 13, 3551–3559.

Neale, R. B., J. H. Richter, and M. Jochum, 2008: The Impact of Convection on ENSO: From a Delayed Oscillator to a Series of Events. *J. Climate*, 21, 5904–5924.

Philander S. G., 1990: *El Niño, La Niña, and the Southern Oscillation*. Academic Press, 289 pp.

Ramanathan V., and W. Collins, 1991: Thermodynamic regulation of ocean warming by cirrus clouds deduced from observations of the 1987 El Niño. *Nature*, **351**, 27–32.

Rasch, P. J., and J. E. Kristjansson, 1998: A comparison of the CCM3 model climate using diagnosed and predicted condensate parameterizations. *J. Climate*, **11**, 1587–1614.

Rayner N. A., D. E. Parker, E. B. Horton, C. K. Folland, L. V. Alexander, D. P. Rowell, E. C. Kent, and A. Kaplan, 2003: Global analyses of sea surface temperature, sea ice and night marine air temperature since the late nineteenth century. *J. Geophys. Res.*, **108**, 4407, doi:10.1029/2002JD002670.

Rodgers, K. B., P. Friederichs, and M. Latif, 2004: Tropical Pacific decadal variability and its relation to decadal modulation of ENSO. *J. Climate*, **17**, 3761–3774.

Schopf, P. S., and R. J. Burgman, 2006: A simple mechanism for ENSO residuals and asymmetry. *J. Climate*, **19**, 3167–3179.

Smith R. D., J. K. Dukowicz, and R. C. Malone, 1992: Parallel ocean general circulation modeling. *Physica D*, **60**, 38–61.

Smith R. D., and P. R. Gent, 2002: Reference manual for the Parallel Ocean Program (POP), ocean component of the Community Climate System Model (CCSM2.0 and 3.0). Los Alamos National Laboratory Tech. Rep. LA-UR-02-2484, 75 pp. [Available online at http://www.ccsm.ucar.edu/models/ccsm3.0/pop.].

Sun D.-Z., and K. E. Trenberth, 1998: Coordinated heat removal from the tropical Pacific region during the 1986–87 El Niño. *Geophys. Res. Lett.,* 25, 2659–2662.

Sun, D.-Z., 2003: A possible effect of an increase in the warm-pool SST on the magnitude of El Niño warming. *J. Climate*, **16**, 185-205.

Sun, D.-Z., T. Zhang, and S.-I. Shin, 2004: The effect of subtropical cooling on the amplitude of ENSO: a numerical study. *J. Climate* , **17**, 3786-3798.

Sun, D.-Z., and T. Zhang, 2006: A Regulatory Effect of ENSO on the Time-Mean Thermal Stratification of the Equatorial Upper Ocean. *Geophys. Res. Lett.*, 33, L07710, doi:10.1029/2005GL025296.

Sun, D.-Z., 2007: The Role of ENSO in Regulating its Background State. In "Nonlinear Dynamics in Geosciences", pages 537-555, Springer New York, 604 pages, Edited by J. Elsner and A. Tsonis.

Sun, D.-Z., T. Zhang, C. Covey, S. A. Klein, W. D. Collins, J. J. Hack, J. T. Kiehl, G. A.

Meehl, I. M. Held, and M. Suarez, 2006: Radiative and Dynamical Feedbacks Over the Equatorial Cold-tongue: Results from Nine Atmospheric GCMs. *J. Climate*, **19**, 4059-4074.

Sun, D.-Z., Y. Yu, and T. Zhang 2009: Tropical Water Vapor and Cloud Feedbacks in Climate Models: A Further Assessment Using Coupled Simulations. *J. Climate*, accepted.

Sun, F., and J.-Y. Yu, 2009: A 10-15year Modulation Cycle of ENSO Intensity. *J. Climate*, **22**, 1718-1735.

Sundqvist H., 1988: Parameterization of condensation and associated clouds in models for weather prediction and general circulation simulation. Physically-based Modeling and Simulation of Climate and Climate Change, Vol. 1, M. E. Schlesinger, Ed., Kluwer Academic, 433–461.

Tang, Y. and W. W. Hsieh, 2003: Nonlinear modes of decadal and interannual variability of the subsurface thermal structure in the Pacific Ocean. *J. Geophys. Res.* 108(C3), 3084, doi:10.1029/2001JC001236.

Trenberth K. E., 1997: The definition of El Niño, *Bull. Am. Meteorol. Soc.,* **78**, 2771-2777.

Uppala, S. M., et al., 2005: The ERA-40 reanalysis, Q. J. R. Meteorol. Soc., 131, 2961–3012, doi:10.1256/qj.04.176/.

Wallace J. M., 1992: Effect of deep convection on the regulation of tropical sea surface temperature. *Nature*, **357**, 230–231.

Xie, P., and P. A. Arkin, 1997: Global precipitation: A 17-year monthly analysis based on gauge observations, satellite estimates, and numerical model outputs, Bull. Am. Meteorol. Soc., 78, 2539–2558.

Zebiak, S. E., and M. A. Cane, 1987: A model El Niño–Southern Oscillation. *Mon. Wea. Rev*, **115**, 2262–2278.

Zhang, G. J., and N. A. McFarlane, 1995: Sensitivity of climate simulations to the parameterization of cumulus convection in the Canadian Climate Centre general circulation model, Atmos. Ocean, 33, 407–446.

Zhang M., W. Lin, C. S. Bretherton, J. J. Hack, and P. J. Rasch, 2003: A modified formulation of fractional stratiform condensation rate in the NCAR Community Atmospheric Model (CAM2). J. Geophys. Res, 108, 4035, doi:10.1029/2002JD002523.

Zhang, T., and D.-Z. Sun, 2006: Response of water vapor and clouds to El Niño warming in three National Center for Atmospheric Research atmospheric models, J. Geophys. Res., 111, D17103, doi:10.1029/2005JD006700.

Table captions

Table 1. Statistics estimated for monthly time series of Niño-3 SST anomalies from observations and five NCAR coupled models. The length of data for computing the statistics is 50 years for all the models and observations (1950–99). The values listed in parentheses are the results from 100-year-long model data and observations (1900-1999).

Table 2. Statistics estimated for monthly time series of equatorial subsurface temperature anomalies from SODA data and five NCAR coupled models. The subsurface temperature anomalies at 75-m depth over the Niño-3 (210°–270°E, 5°S–5°N) region (Tsub_Nino3), at 150-m depth over the western Pacific (130°–170°E, 5°S–5°N) (Tsub_WP), and from the difference between them (Tsub_diff) are used in the calculation. The length of data for computing the statistics is 50 years for all the five models and SODA data (1950–99).

Figure captions

Figure 1. Histograms of the monthly mean Niño-3 SST anomalies from observations and five NCAR coupled models. The normal distributions with the respective standard deviation are plotted as dashed line. A bin width of 0.2^{o}C is used. The length of data used in the calculation is 50 years for all the models and observations (1950–99).

Figure 2. Spatial distributions of composite SST anomalies during El Niño (left panel) and La Niña (right panel) events from observations and five NCAR coupled models. The positive (negative) anomalies of Niño-3 SST with a value greater than 0.5^{o}C (-0.5^{o}C) are selected to construct composites of warm (cold) events. The length of data used in the calculation is 50 years for all the NCAR models and observations (1950–99). Shading indicates that the anomalies are statistically significant at the 95% confidence level using the *t* test.

Figure 3. Spatial distributions of the asymmetry between El Niño and La Niña events from observations and five NCAR coupled models. The left panel is the sum of of El Niño and La Niña composite SST anomalies, and the right panel is the skewness pattern of SST anomalies (contour) overlaid with the difference in SST climatology between models and observations (shaded). The positive (negative) anomalies of Niño-3 SST

with a value greater than 0.5°C (-0.5°C) are selected to construct composites of warm (cold) events. The length of data used in the calculation is 50 years for all the models and observations (1950–99).

Figure 4. The composite anomalies of equatorial (5°S-5°N) upper ocean temperature during warm periods (left panel) and cold periods (right panel). The length of data used in the calculation is 50 years for all the five models and SODA data (1950–99). Shading indicates that the anomalies are statistically significant at the 95% confidence level using the *t* test.

Figure 5. Time-mean equatorial (5°S-5°N) upper ocean temperature from five models and SODA data. The 20 °C isotherm is plotted as red solid line in the figure. The length of data used in the calculation is 50 years for all the five models and SODA data (1950–99).

Figure 6. Spatial distributions of 20 °C isotherm depth anomalies during warm periods (left panel) and cold periods (right panel). The length of data used in the calculation is 50 years for all the five models and SODA data (1950-1999). Shading indicates that the anomalies are statistically significant at the 95% confidence level using the *t* test.

Figure 7. The asymmetry in the equatorial upper ocean temperature (left panel) and in 20 ^{o}C isotherm depth (right panel). Shown are the results from the sum between warm anomalies and cold anomalies. The length of data used in the calculation is 50 years for all the five models and SODA data (1950-1999).

Figure 8. The asymmetry in meridional cross sections of the upper ocean temperature over the western Pacific (130°–170°E) (left panel) and Niño-3 region (210°–270°E) (right panel). Shown are the results from the sum between warm anomalies and cold anomalies. The length of data used in the calculation is 50 years for all the five models and SODA data (1950-1999).

Figure 9. Histograms of the monthly mean Niño-3 subsurface temperature anomalies at 75-m depth. The normal distributions with the respective standard deviation are plotted as dashed line. A bin width of 0.2^{o}C is used. The length of data used in the calculation is 50 years for all the models and SODA data (1950–99).

Figure 10. Spatial distributions of net surface heat flux anomalies during warm periods (left panel) and cold periods (right panel). The length of data used in the calculation is 50 years for all the NCAR models and 45 years for the ERA-40 (September 1957-August 2002). Shading indicates that the anomalies are statistically significant at

the 95% confidence level using the *t* test.

Figure 11. Scatter plot between the net surface heat flux anomalies and the SST anomalies over the Niño-3 region (left panel) and the spatial distributions of asymmetry in net surface heat flux (right panel). The corresponding slope values of linear regression for positive and negative SST anomalies are listed in the top and bottom, respectively. The asymmetry in net surface heat flux is defined as the sum between warm anomalies and cold anomalies. The length of data used in the calculation is 50 years for all the models and 45 years for the ERA-40 (September 1957-August 2002).

Figure 12. Spatial distributions of precipitation anomalies during warm periods (left panel) and cold periods (right panel). The length of data used in the calculation is 50 years for all the NCAR models and 28 years for the CMAP precipitation (1979-2006). Shading indicates that the anomalies are statistically significant at the 95% confidence level using the *t* test.

Figure 13. Spatial distributions of zonal wind stress anomalies during warm periods (left panel) and cold periods (right panel). The length of data used in the calculation is 50 years for all the NCAR models and about 48 years for SODA zonal wind stress

(January 1958- November 2005). Shading indicates that the anomalies are statistically significant at the 95% confidence level using the *t* test.

Figure 14. Spatial distributions of asymmetry in precipitation (left panel) and in zonal wind stress (right panel). Shown are the results from the sum between warm anomalies and cold anomalies. The length of data used in the calculation is 50 years for all the models and about 48 years for SODA zonal wind stress (January 1958-November 2005), and 28 years for the CMAP precipitation (1979-2006).

Figure 15. Same as in Figure 14, but for the corresponding AMIP runs. Shown are the results from the longest corresponding AMIP runs available to us, whose periods used in the calculation are respectively Feb. 1979—Jan. 1993 for CCSM1, January 1950—December 1999 for CCSM2, January 1979—December 1999 for CCSM3-T42, January 1979—December 2000 for CCSM3-T85, and January 1977—December 2002 for CCSM3+NR. The AMIP runs for the four old versions used in this study are the same as those used by Sun et al. (2009).

Figure 16: Same as in Figure 12, but for the corresponding AMIP runs. Shading indicates that the anomalies are statistically significant at the 95% confidence level

using the *t* test.

Figure 17: Same as in Figure 13, but for the corresponding AMIP runs. Shading indicates that the anomalies are statistically significant at the 95% confidence level using the *t* test.

Table 1. Statistics estimated for monthly Niño-3 time series from observations and five NCAR coupled models. The length of data for computing the statistics is 50 years for all the models and observations (1950–99). The values listed in parentheses are the results from 100-year-long model data and observations (1900-1999).

Source	standard deviation	skewness
Observed	0.88 ^{O}C (0.82)	0.86 (0.62)
CCSM1	0.47 ^{O}C (0.47)	0.36 (0.31)
CCSM2	0.92 ^{O}C (0.92)	0.012 (0.052)
CCSM3	0.81 ^{O}C (0.84)	0.089 (-0.10)
CCSM3(T85)	0.79 ^{O}C (0.85)	-0.13 (-0.20)
CCSM3+NR	1.03 ^{O}C (1.12)	0.31 (0.17)

Table 2. Statistics estimated for monthly time series of equatorial subsurface temperature anomalies from SODA data and five NCAR coupled models. The subsurface temperature anomalies at 75-m depth over the Niño-3 (210°–270°E, 5°S–5°N) region (Tsub_Nino3), at 150-m depth over the western Pacific (130°–170°E, 5°S–5°N) (Tsub_WP), and from the difference between them (Tsub_diff) are used in the calculation. The length of data for computing the statistics is 50 years for all the five models and SODA data (1950–99).

Source	standard deviation (^{O}C)			skewness		
	Tsub_WP	Tsub_Nino3	Tsub_diff	Tsub_WP	Tsub_Nino3	Tsub_diff
Observed	1.36	1.51	2.44	-0.18	0.45	0.61
CCSM1	0.36	0.37	0.53	0.038	0.063	-0.065
CCSM2	1.21	0.77	1.53	0.016	0.15	0.089
CCSM3	1.10	1.00	1.66	0.092	0.23	-0.22
CCSM3(T85)	1.08	0.81	1.54	0.10	0.21	0.010
CCSM3+NR	1.42	1.36	2.36	0.22	0.24	0.11

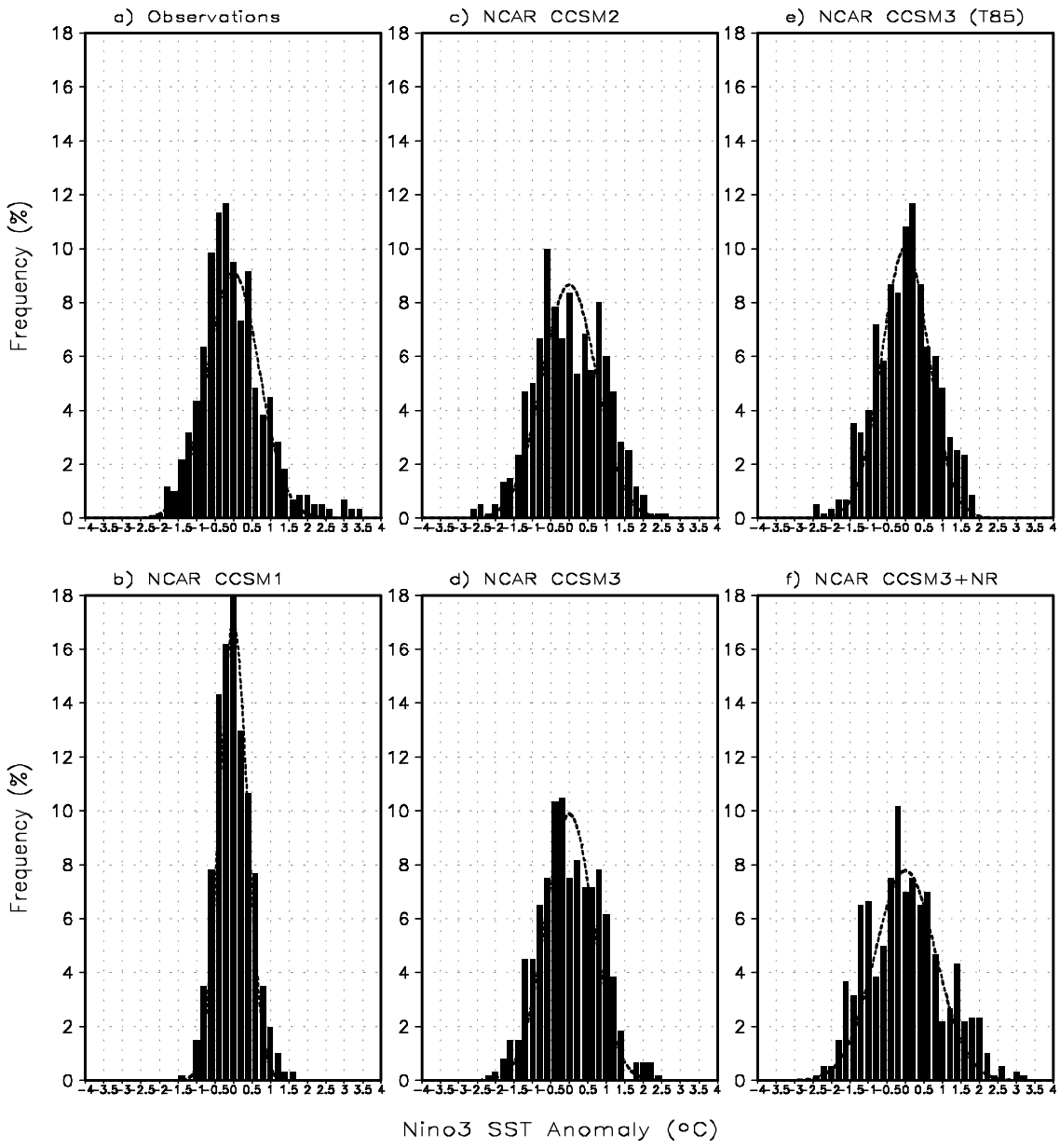

Figure 1. Histograms of the monthly mean Niño-3 SST anomalies from observations and five NCAR coupled models. The normal distributions with the respective standard deviation are plotted as dashed line. A bin width of 0.2°C is used. The length of data used in the calculation is 50 years for all the models and observations (1950–99).

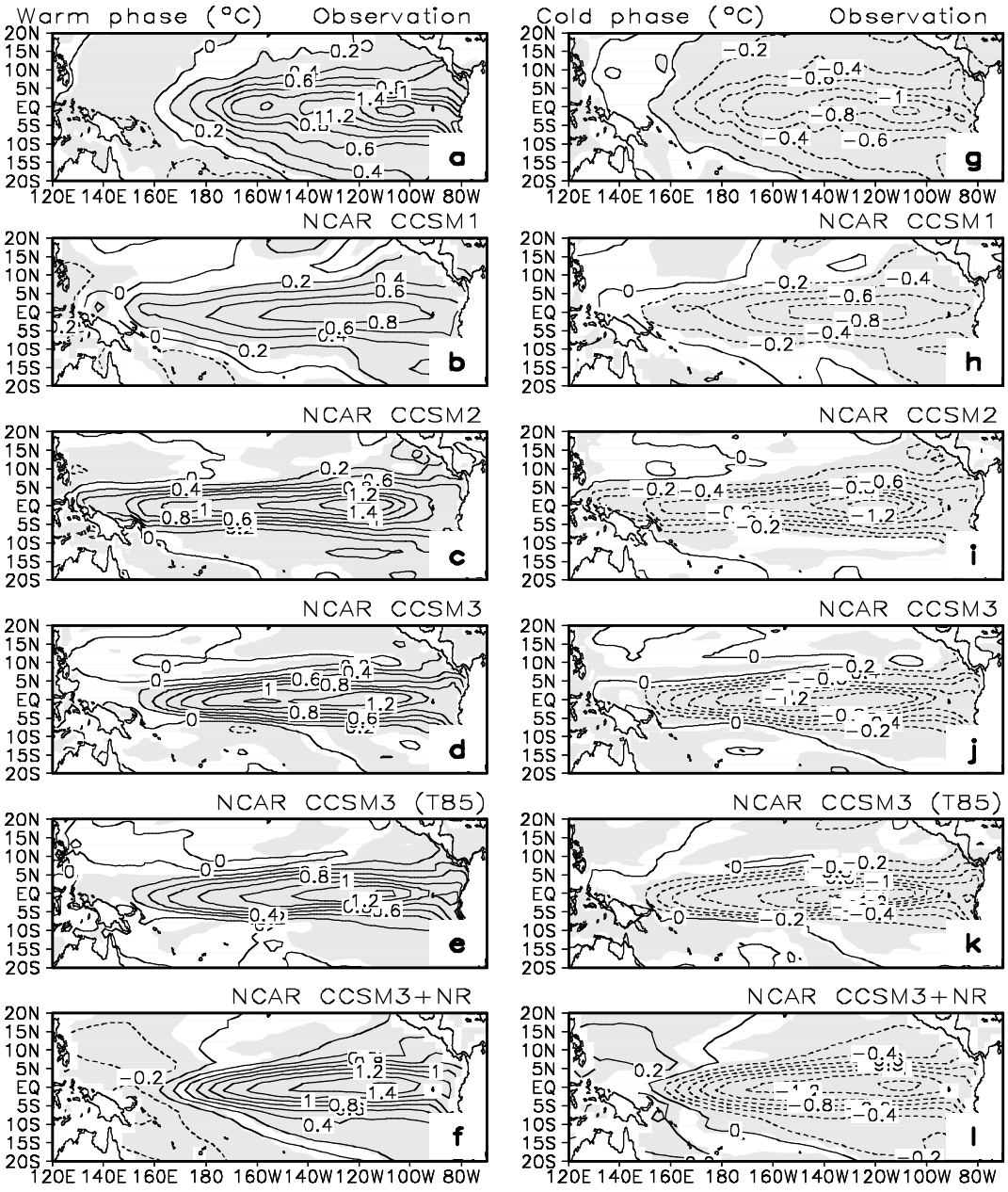

Figure 2. Spatial distributions of composite SST anomalies during El Niño (left panel) and La Niña (right panel) events from observations and five NCAR coupled models. The positive (negative) anomalies of Niño-3 SST with a value greater than 0.5°C (-0.5°C) are selected to construct composites of warm (cold) events. The length of data used in the calculation is 50 years for all the NCAR models and observations (1950–99). Shading indicates that the anomalies are statistically significant at the 95% confidence level using the *t* test.

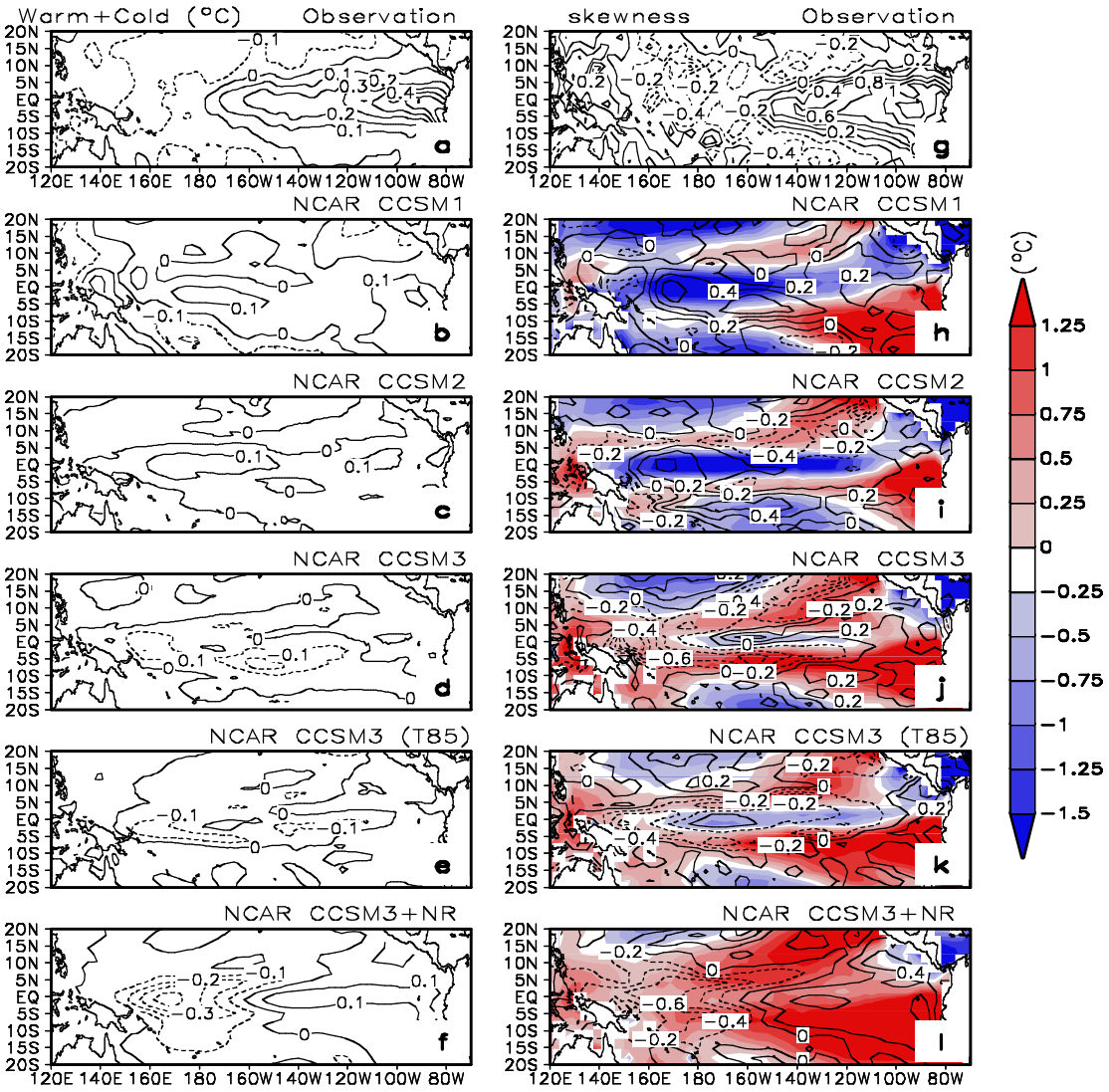

Figure 3. Spatial distributions of the asymmetry between El Niño and La Niña events from observations and five NCAR coupled models. The left panel is the sum of of El Niño and La Niña composites, and the right panel is the skewness pattern of SST anomalies (contour) overlaid with the difference in SST climatology between models and observations (shaded). The positive (negative) anomalies of Niño-3 SST with a value greater than 0.5°C (-0.5°C) are selected to construct composites of warm (cold) events. The length of data used in the calculation is 50 years for all the models and observations (1950–99).

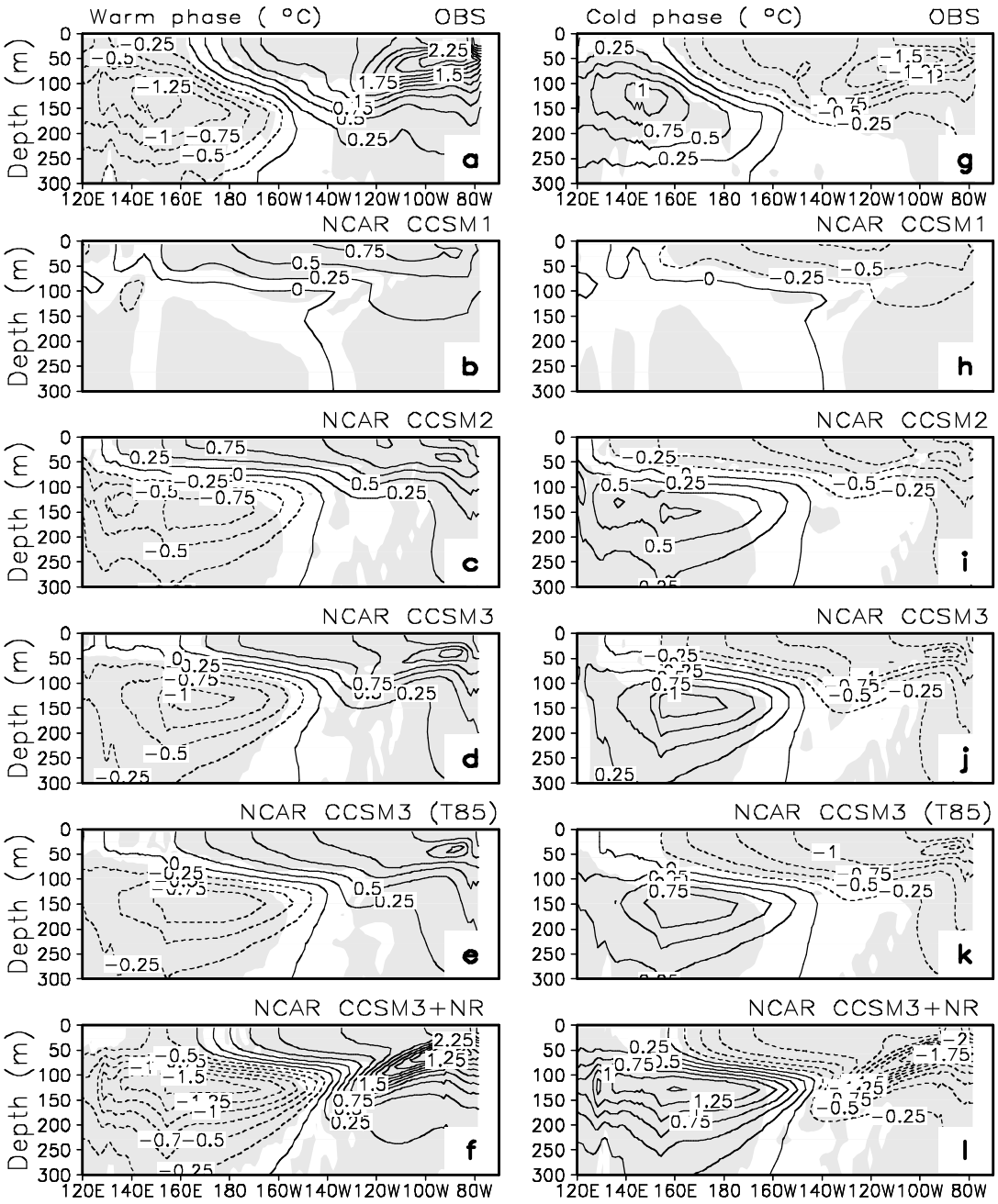

Figure 4. The composite anomalies of equatorial (5°S-5°N) upper ocean temperature during warm periods (left panel) and cold periods (right panel). The length of data used in the calculation is 50 years for all the five models and SODA data (1950–99). Shading indicates that the anomalies are statistically significant at the 95% confidence level using the *t* test.

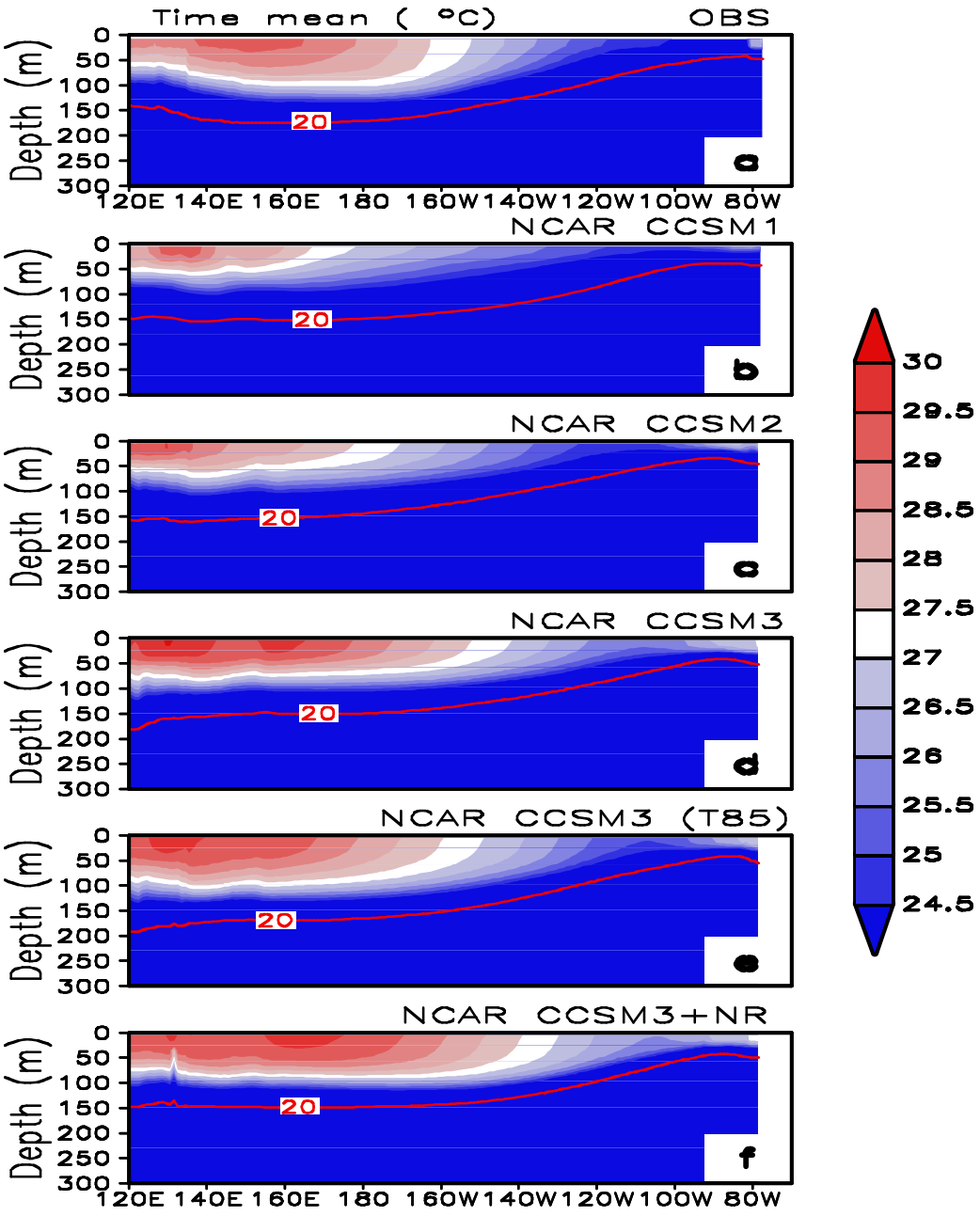

Figure 5. Time-mean equatorial (5°S-5°N) upper ocean temperature from five models and SODA data. The 20 °C isotherm is plotted as red solid line in the figure. The length of data used in the calculation is 50 years for all the five models and SODA data (1950–99).

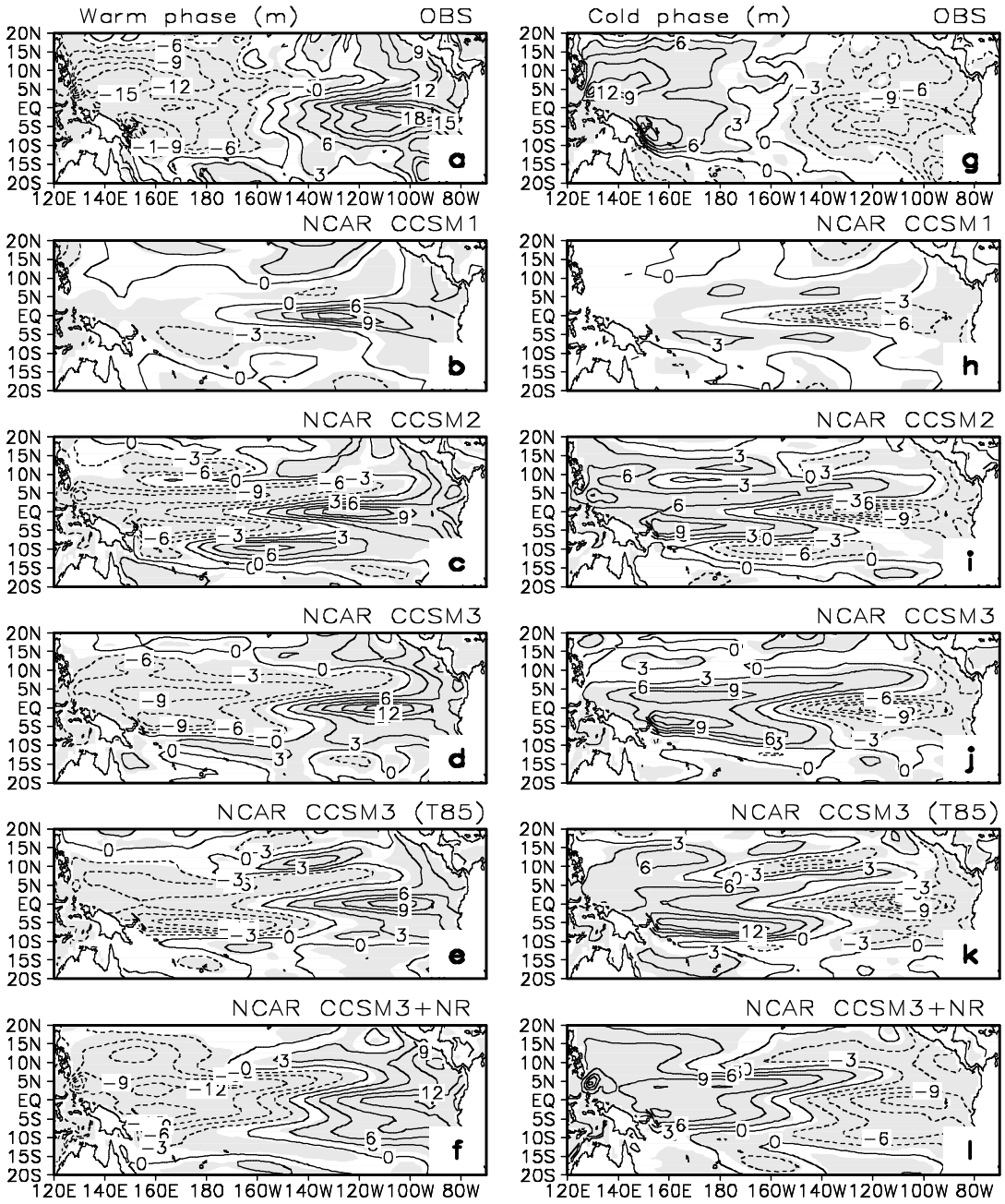

Figure 6. Spatial distributions of 20 °C isotherm depth anomalies during warm periods (left panel) and cold periods (right panel). The length of data used in the calculation is 50 years for all the five models and SODA data (1950-1999). Shading indicates that the anomalies are statistically significant at the 95% confidence level using the *t* test.

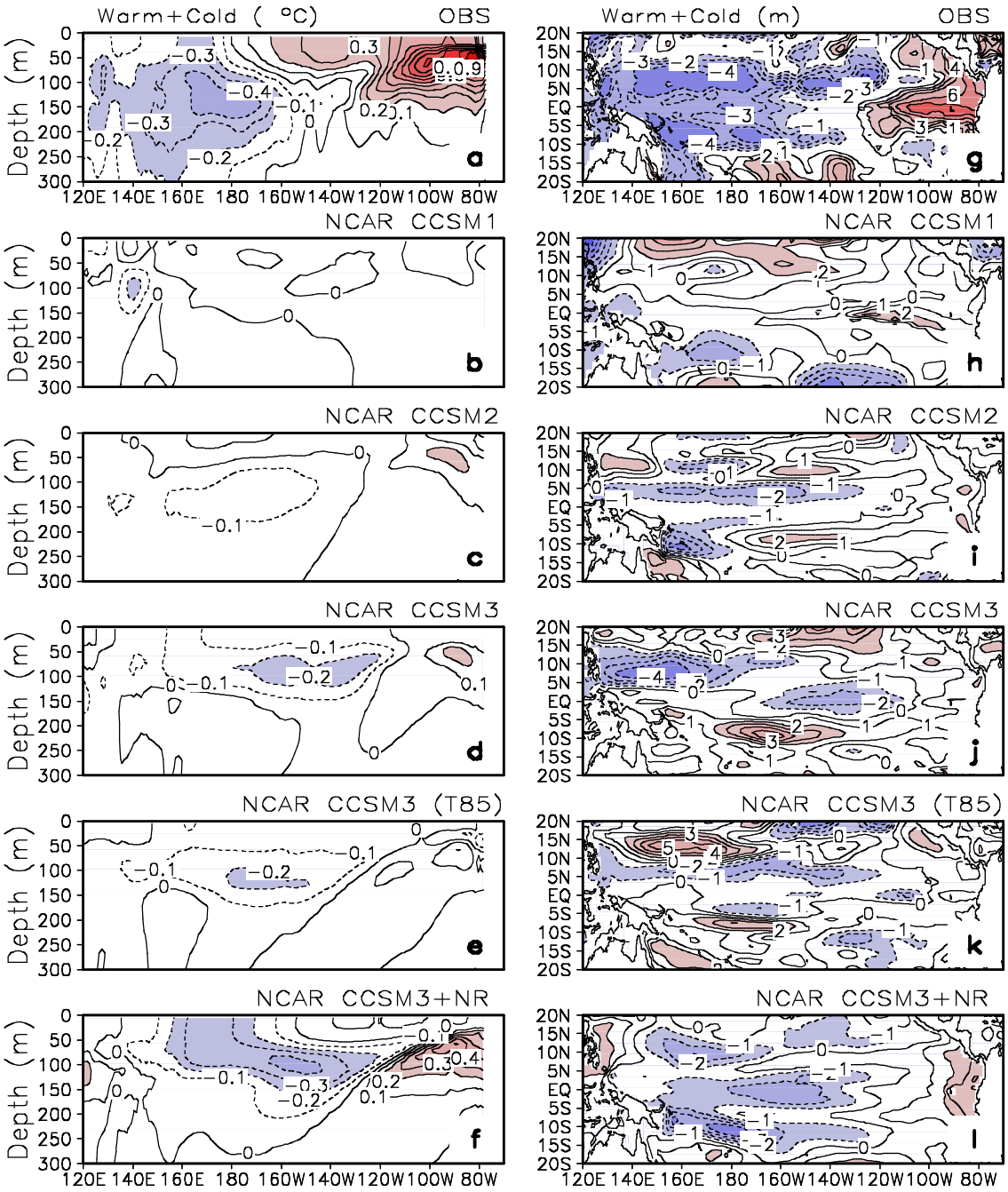

Figure 7. The asymmetry in the equatorial upper ocean temperature (left panel) and in 20 °C isotherm depth (right panel). Shown are the results from the sum between warm anomalies and cold anomalies. The length of data used in the calculation is 50 years for all the five models and SODA data (1950-1999).

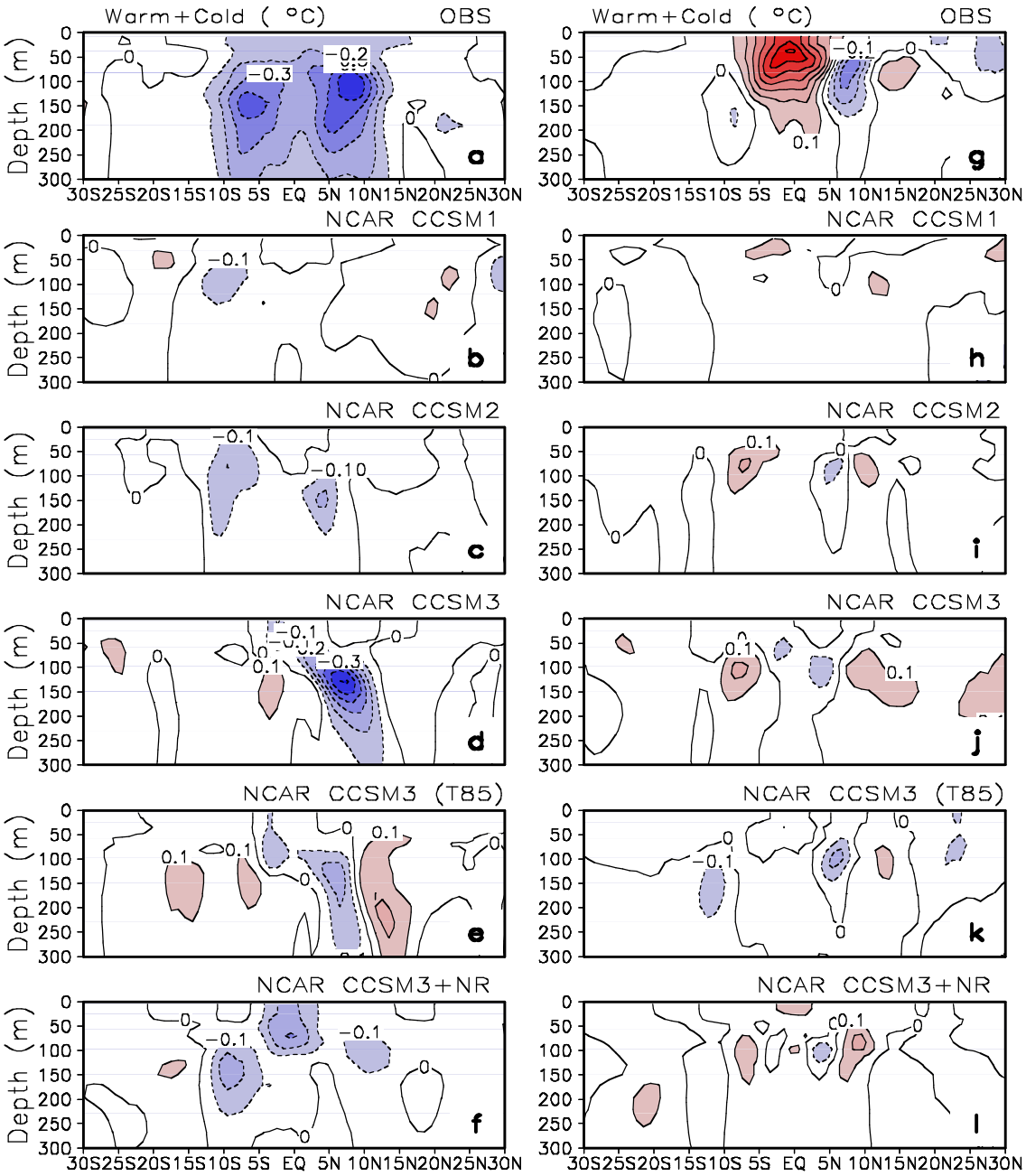

Figure 8. The asymmetry in meridional cross sections of the upper ocean temperature over the western Pacific (130°–170°E) (left panel) and Niño-3 region (210°–270°E) (right panel). Shown are the results from the sum between warm anomalies and cold anomalies. The length of data used in the calculation is 50 years for all the five models and SODA data (1950-1999).

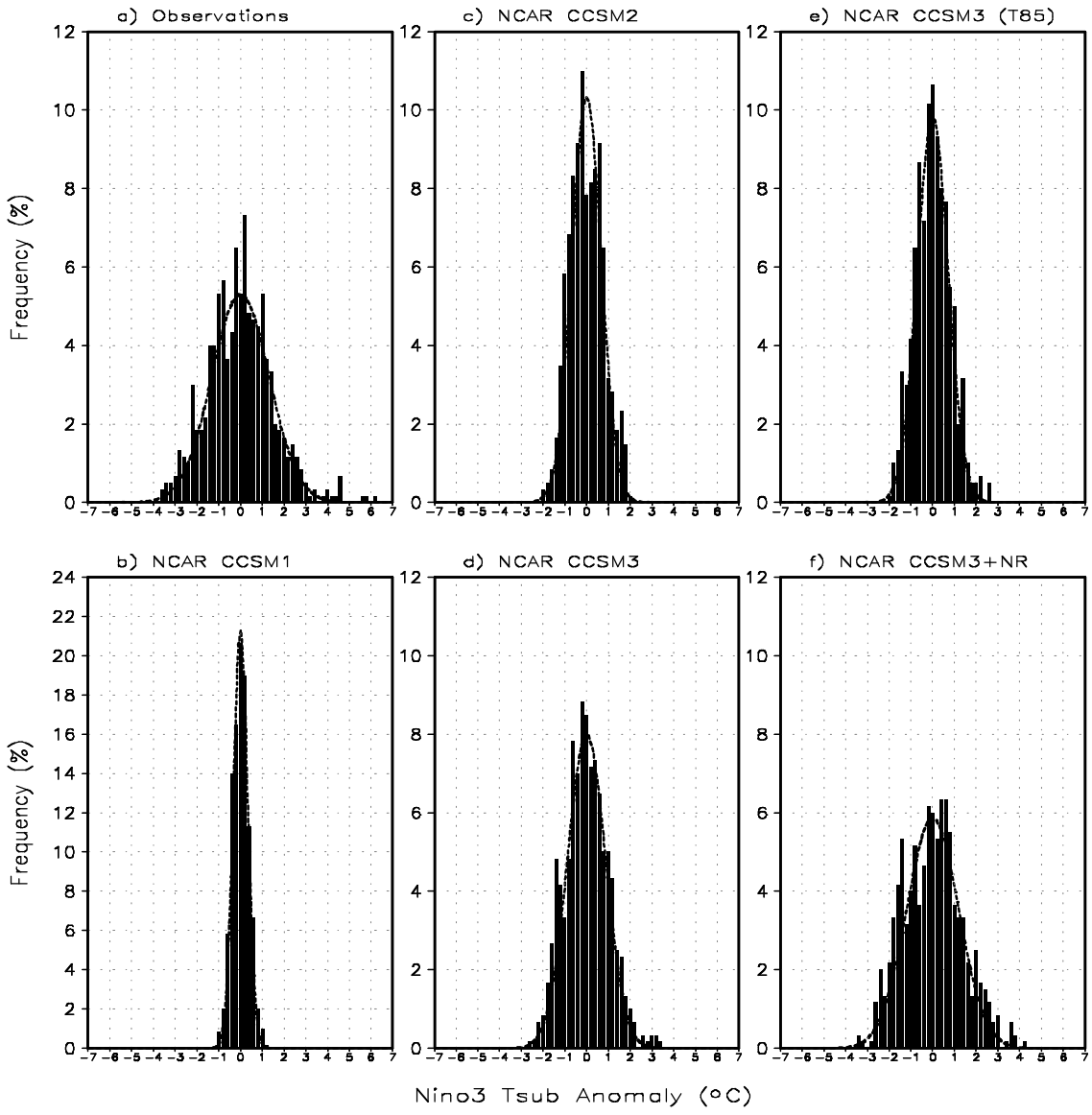

Figure 9. Histograms of the monthly mean Niño-3 subsurface temperature anomalies at 75-m depth. The normal distributions with the respective standard deviation are plotted as dashed line. A bin width of 0.2°C is used. The length of data used in the calculation is 50 years for all the models and SODA data (1950–99).

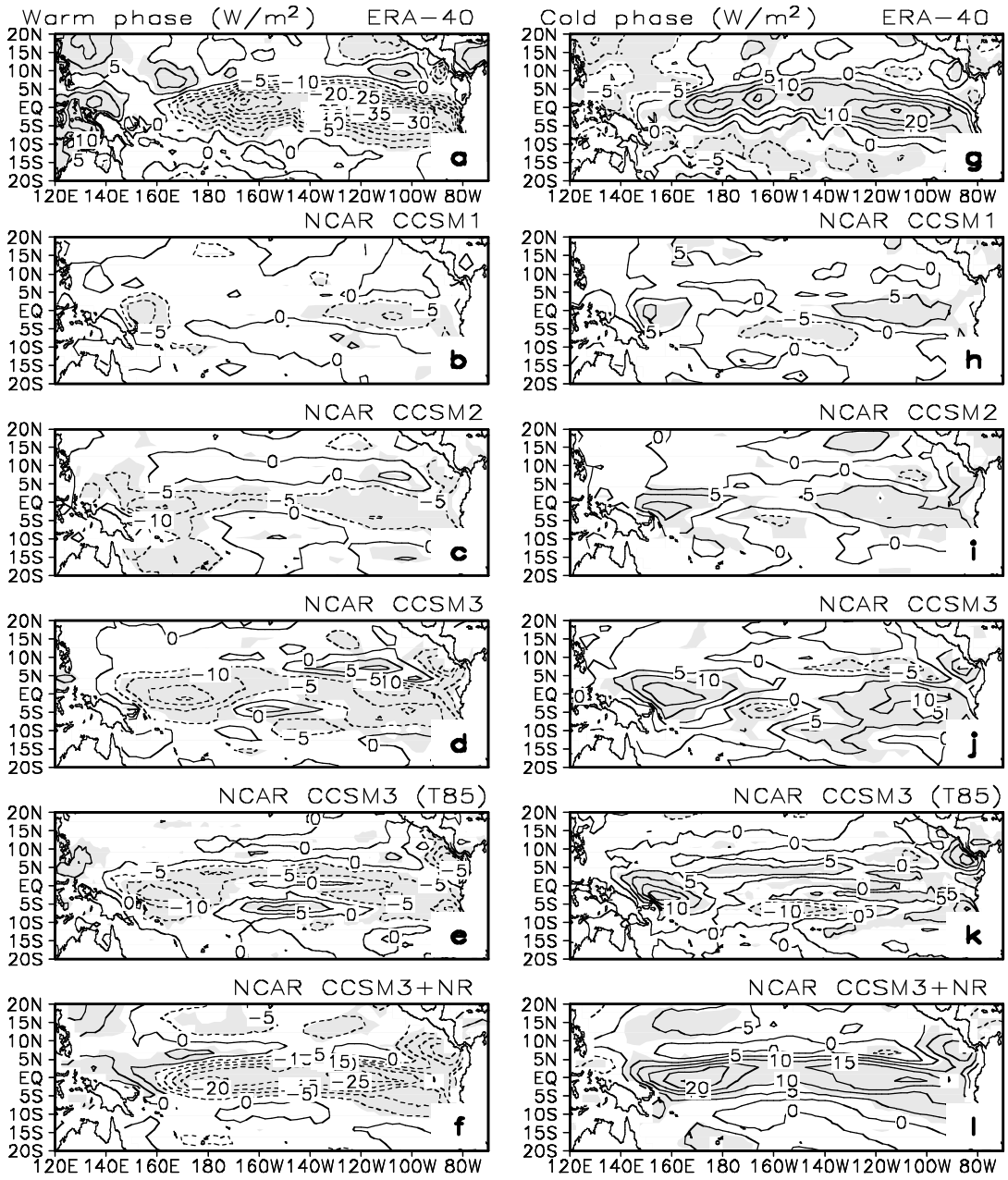

Figure 10. Spatial distributions of net surface heat flux anomalies during warm periods (left panel) and cold periods (right panel). The length of data used in the calculation is 50 years for all the NCAR models and 45 years for the ERA-40 (September 1957-August 2002). Shading indicates that the anomalies are statistically significant at the 95% confidence level using the *t* test.

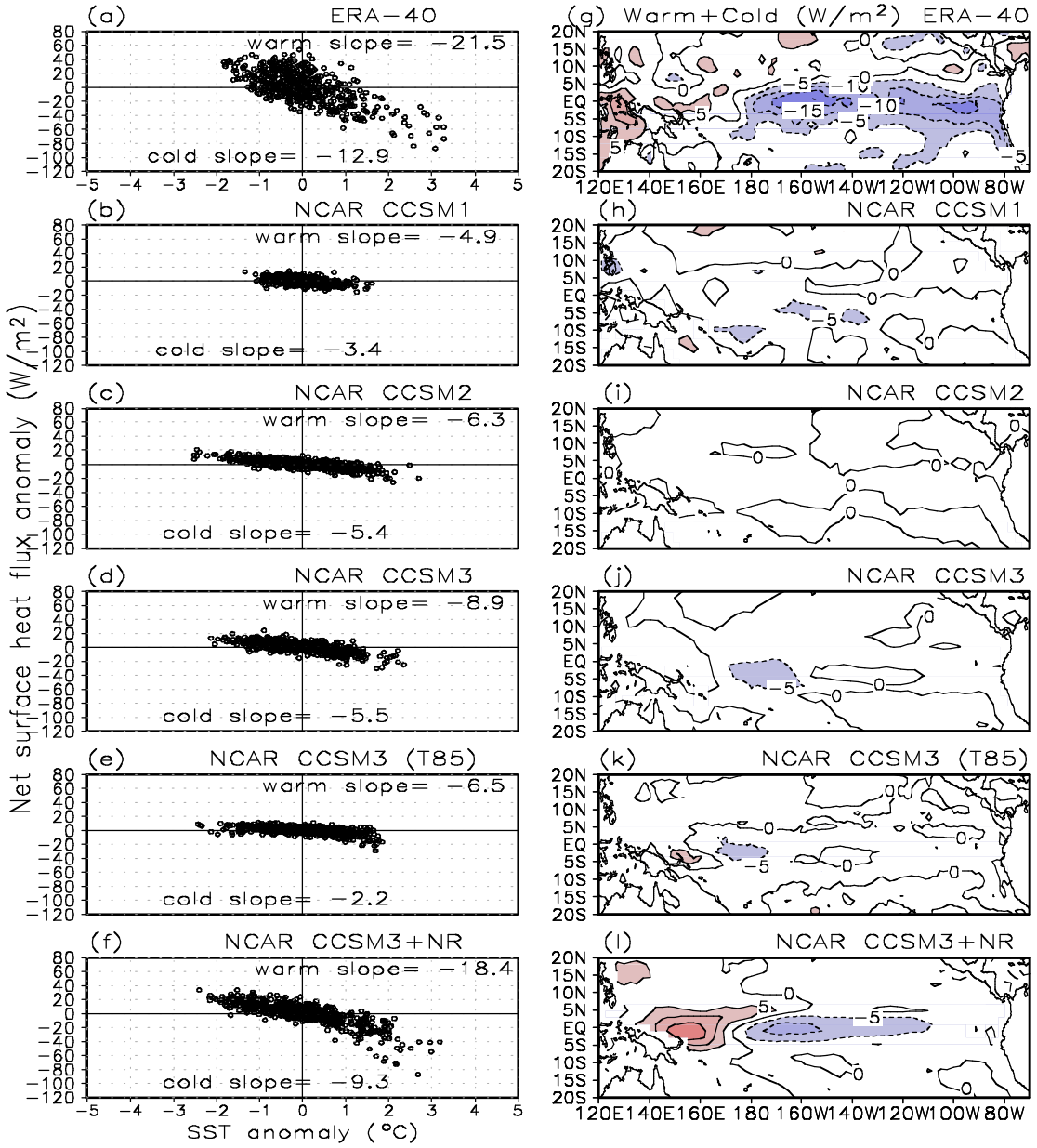

Figure 11. Scatter plot between the net surface heat flux anomalies and the SST anomalies over the Niño-3 region (left panel) and the spatial distributions of asymmetry in net surface heat flux (right panel). The corresponding slope values of linear regression for positive and negative SST anomalies are listed in the top and bottom, respectively. The asymmetry in net surface heat flux is defined as the sum between warm anomalies and cold anomalies. The length of data used in the calculation is 50 years for all the models and 45 years for the ERA-40 (September 1957-August 2002).

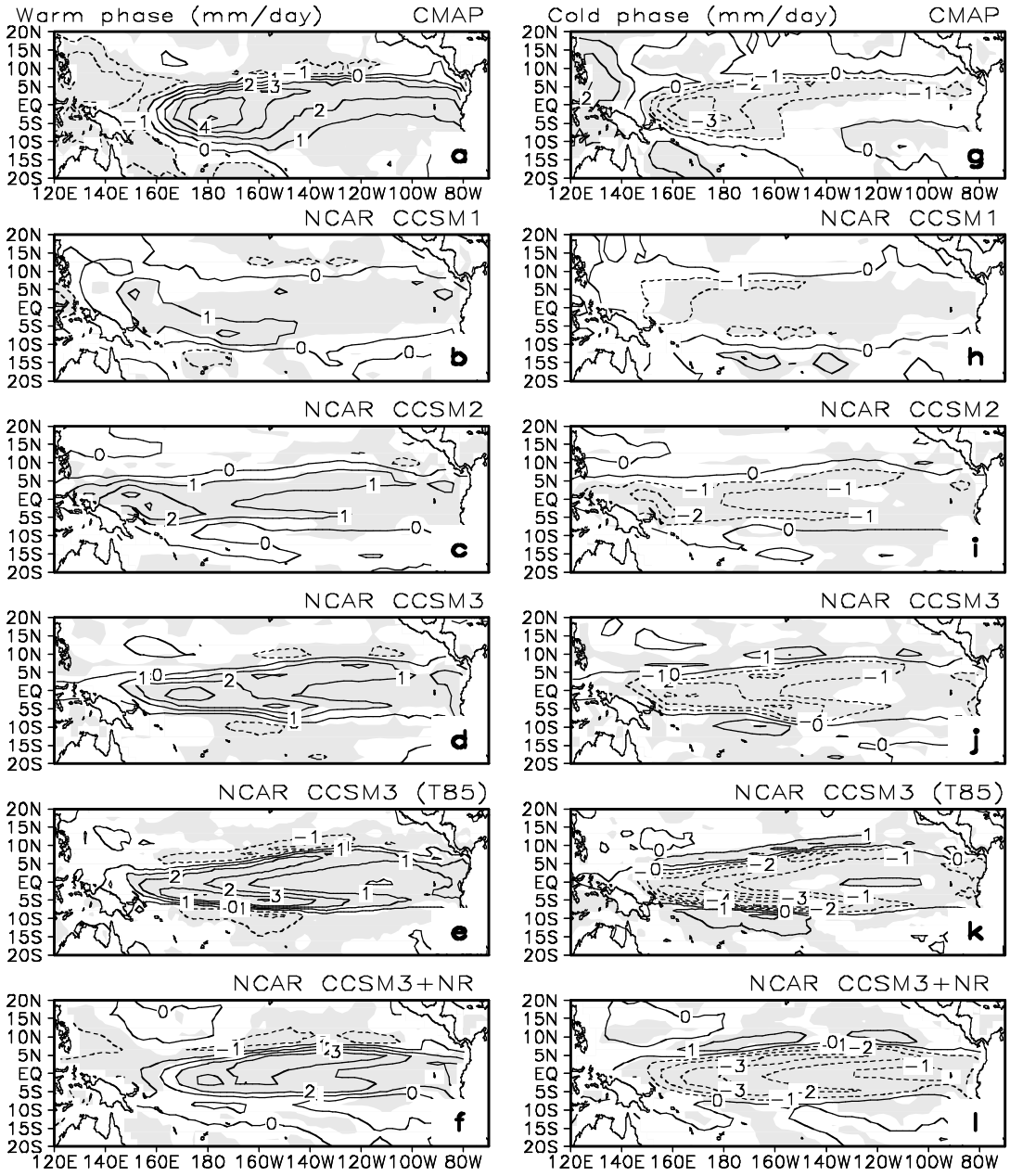

Figure 12. Spatial distributions of precipitation anomalies during warm periods (left panel) and cold periods (right panel). The length of data used in the calculation is 50 years for all the NCAR models and 28 years for the CMAP precipitation (1979-2006). Shading indicates that the anomalies are statistically significant at the 95% confidence level using the *t* test.

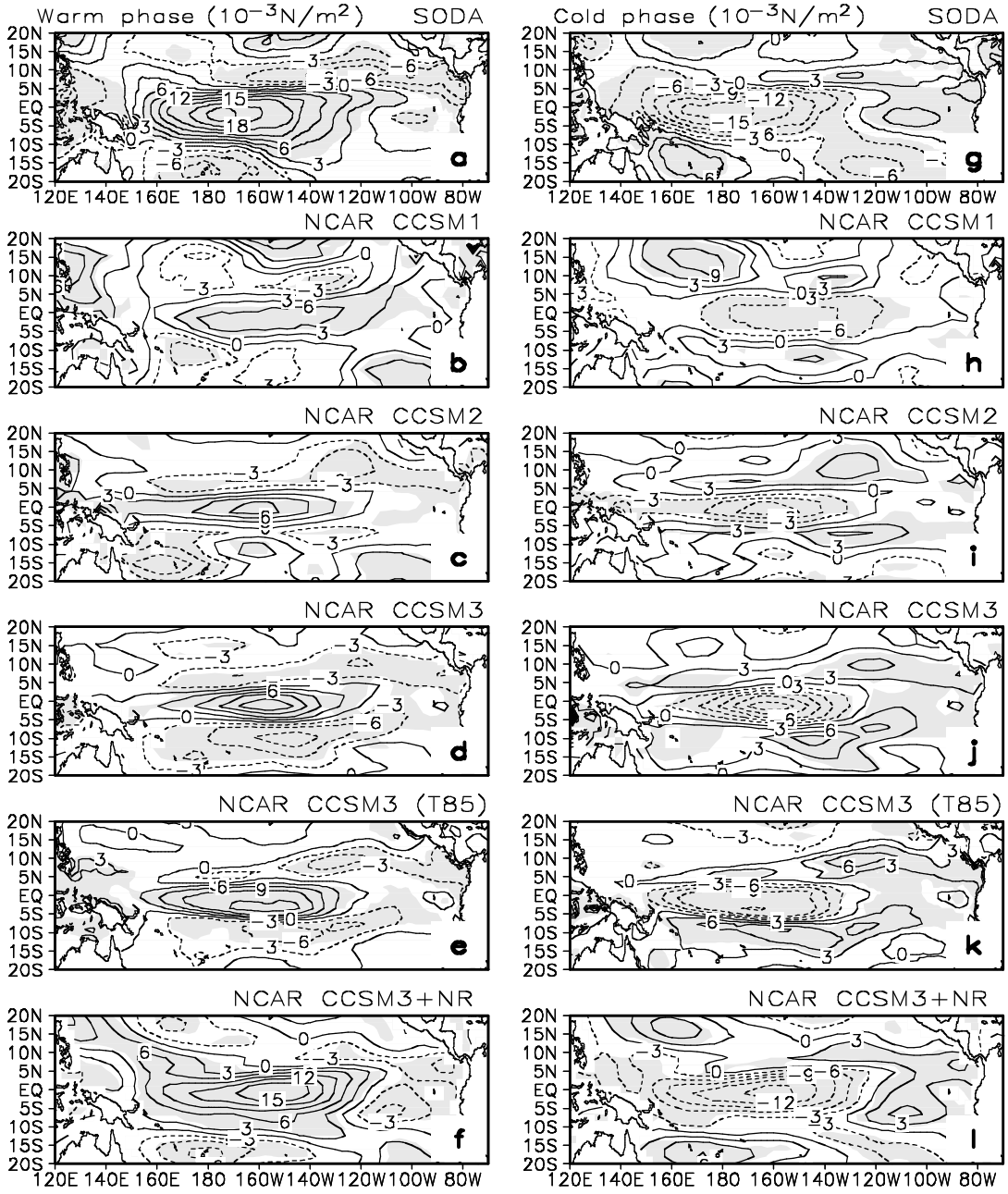

Figure 13. Spatial distributions of zonal wind stress anomalies during warm periods (left panel) and cold periods (right panel). The length of data used in the calculation is 50 years for all the NCAR models and about 48 years for SODA zonal wind stress (January 1958- November 2005). Shading indicates that the anomalies are statistically significant at the 95% confidence level using the *t* test.

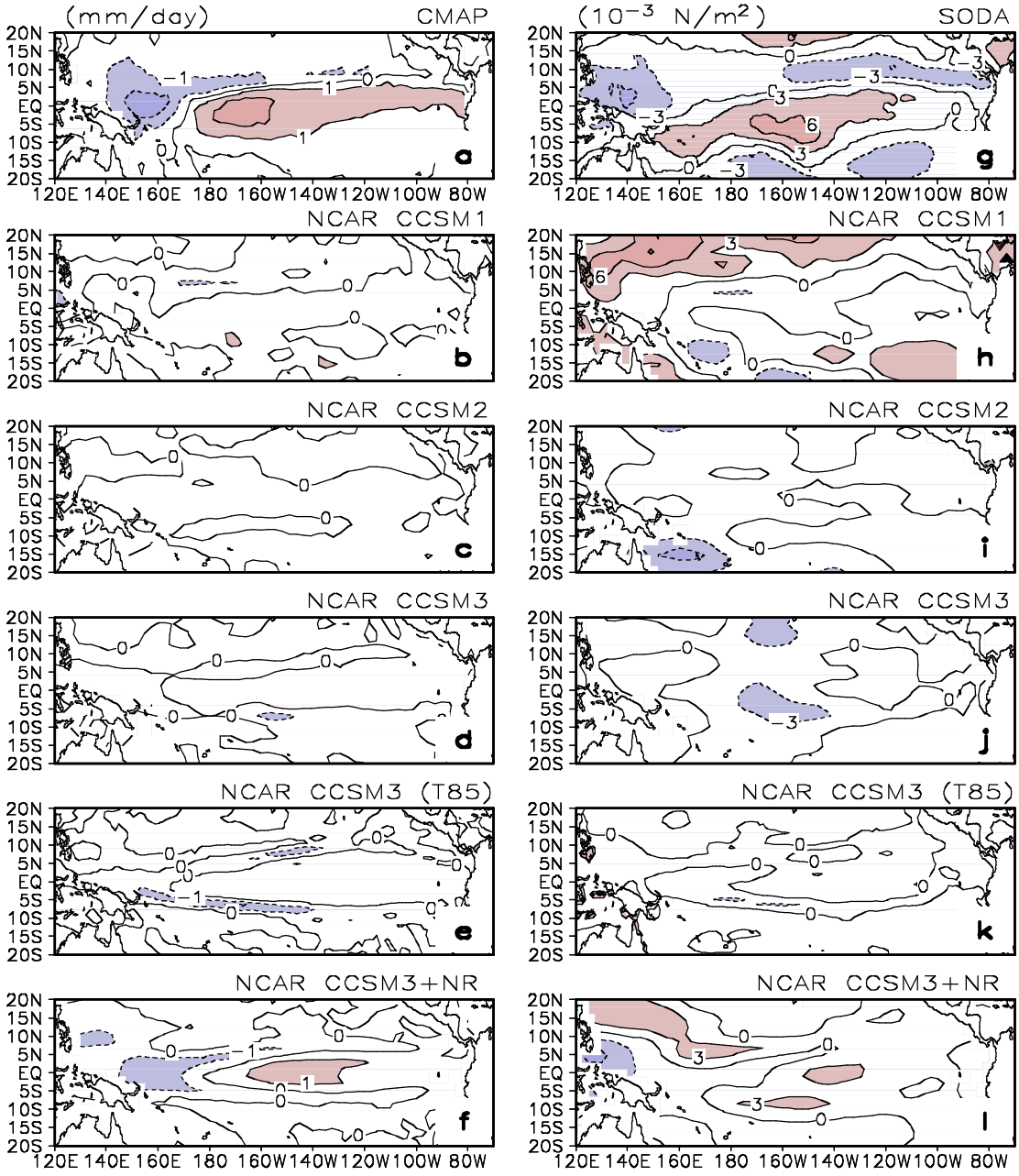

Figure 14. Spatial distributions of asymmetry in precipitation (left panel) and in zonal wind stress (right panel). Shown are the results from the sum between warm anomalies and cold anomalies. The length of data used in the calculation is 50 years for all the models and about 48 years for SODA zonal wind stress (January 1958-November 2005), and 28 years for the CMAP precipitation (1979-2006).

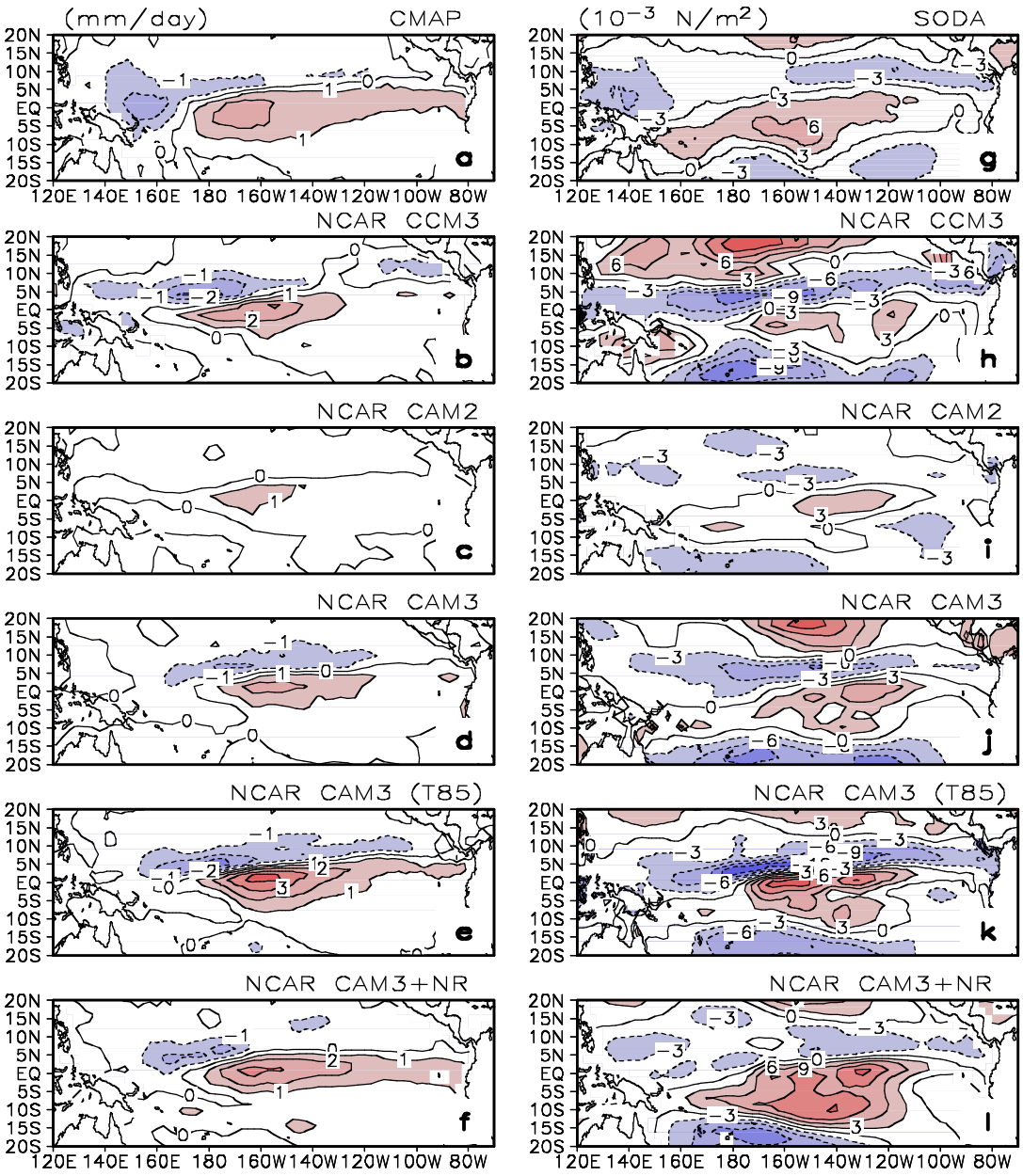

Figure 15. Same as in Figure 14, but for the corresponding AMIP runs. Shown are the results from the longest corresponding AMIP runs available to us, whose periods used in the calculation are respectively Feb. 1979—Jan. 1993 for CCSM1, January 1950—December 1999 for CCSM2, January 1979—December 1999 for CCSM3-T42, January 1979—December 2000 for CCSM3-T85, and January 1977—December 2002 for CCSM3+NR. The AMIP runs for the four old versions used in this study are the same as those used by Sun et al. (2009).

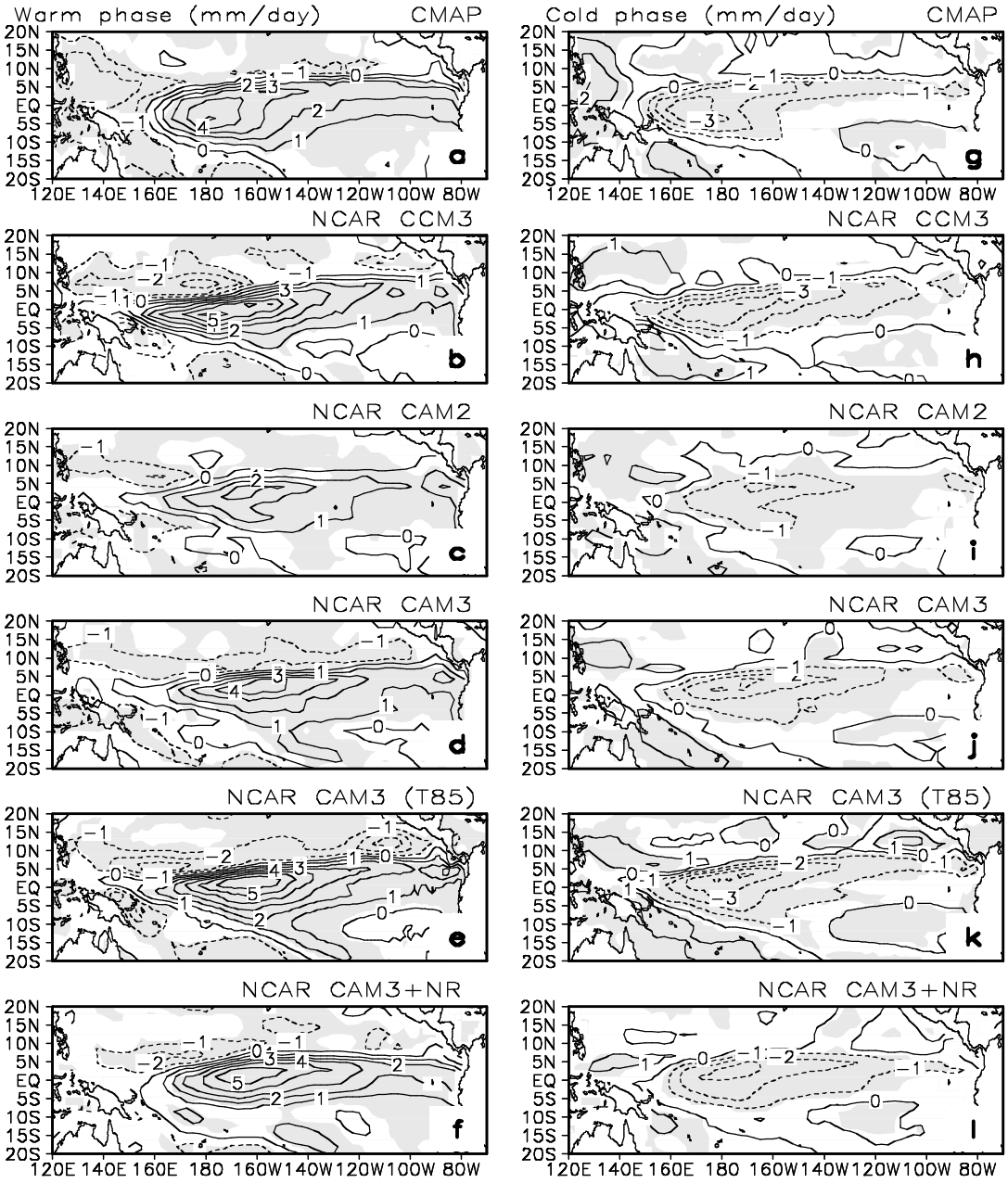

Figure 16: Same as in Figure 12, but for the corresponding AMIP runs. Shading indicates that the anomalies are statistically significant at the 95% confidence level using the *t* test.

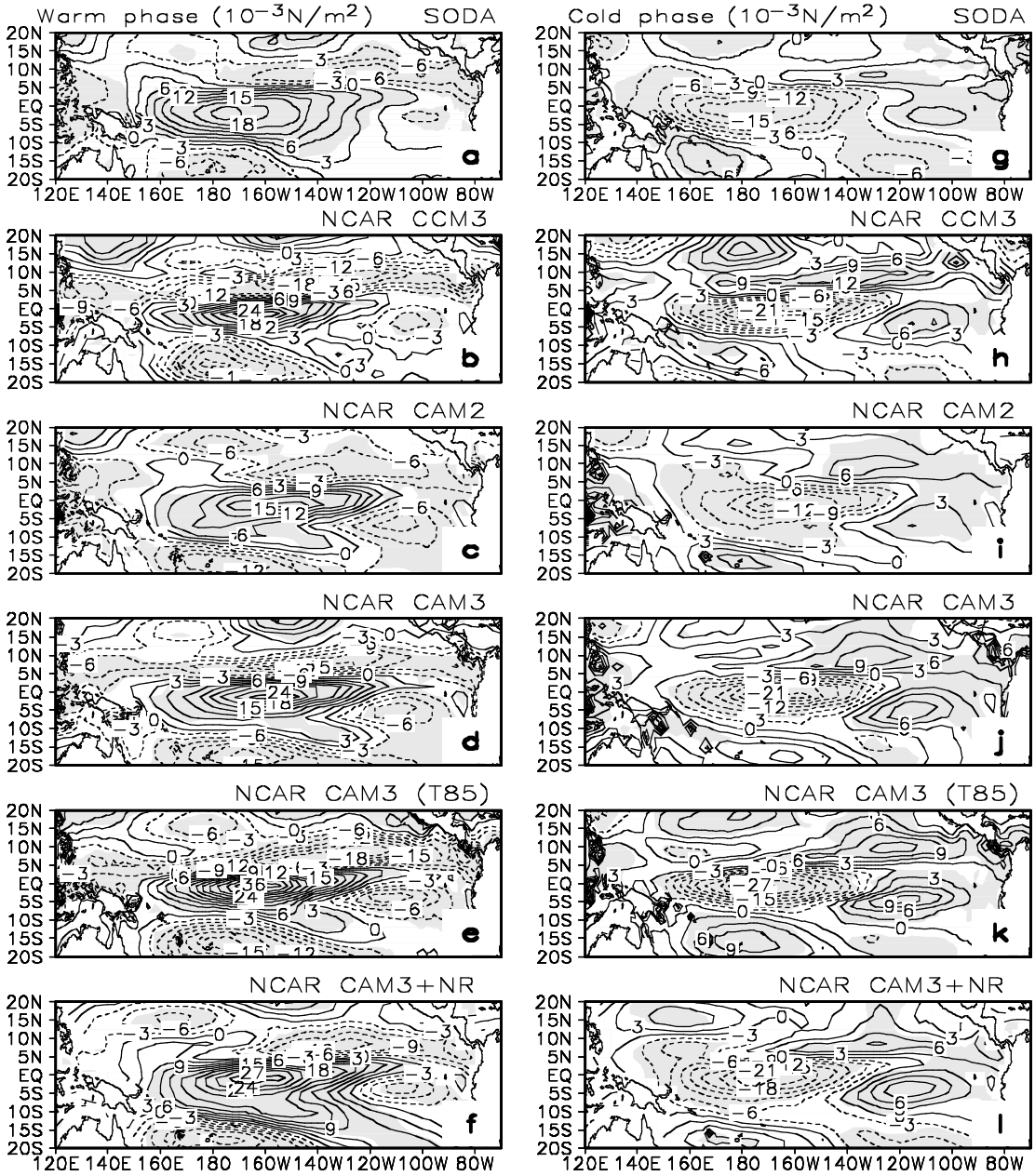

Figure 17: Same as in Figure 13, but for the corresponding AMIP runs. Shading indicates that the anomalies are statistically significant at the 95% confidence level using the *t* test.